Journal of Structural Geology 147 (2021) 104326

Contents lists available at ScienceDirect

Journal of Structural Geology

journal homepage: http://www.elsevier.com/locate/jsg

Unveiling ductile deformation during fast exhumation of a granitic pluton in a transfer zone

Richard Spiess [a,*], Antonio Langone [b], Alfredo Caggianelli [c], Finlay M. Stuart [d], Martina Zucchi [c], Caterina Bianco [c], Andrea Brogi [c,e], Domenico Liotta [c,e]

[a] Department of Geosciences, University of Padova, Italy
[b] CNR-IGG, Institute of Geosciences and Earth Resources, Pavia, Italy
[c] Department of Earth and Geoenvironmental Sciences, University of Bari, Italy
[d] Isotope Geosciences, Scottish Universities Environmental Research Centre, East Kilbride, UK
[e] CNR-IGG, Institute of Geosciences and Earth Resources, Pisa, Italy

ARTICLE INFO

Keywords:
Granite emplacement
Fast exhumation
Extensional tectonics
Shearing
Geochronology –thermochronology
Rheological modeling

ABSTRACT

Exhumation and cooling of upper crustal plutons is generally assumed to develop in the brittle domain, thus determining an abrupt passage from crystallization to faulting. To challenge this general statement, we applied an integrated approach involving meso- and micro-structural studies, thermochronology, geochronology and rheological modeling to the Miocene syn-tectonic Porto Azzurro pluton on Elba (Tuscan archipelago – Italy). This pluton is emplaced in an extensional setting, and we have realized that its fast exhumation is accompanied by localized ductile shear zones, developing along dykes and veins, later affected by brittle deformation. This is unequivocally highlighted by field studies and EBSD-aided microstructural analysis. To constrain the emplacement and exhumation rate of the Porto Azzurro pluton we performed U–Pb zircon dating and (U + Th)/He apatite thermochronology, which resulted in a magma emplacement age of 6.4 ± 0.4 Ma and an exhumation rate of 3.4–3.9 mm/yr. Thermo-rheological modeling established that localized ductile deformation occurred at two different time steps: within felsic dykes when the pluton first entered into the brittle field at 380 kyr, and along quartz-rich hydrothermal veins at c. 550 kyr after pluton emplacement. Hence, the major conclusion of our data is that ductile deformation can affect a granitic intrusion even when it is entered into the brittle domain in a fast exhuming extensional regime.

1. Introduction

If strain rate is high ($\geq 1*10^{-14}$ s^{-1}, Ranalli, 1995; Rey et al., 2009), extensional tectonics can be accompanied by high heat flow and diffuse emplacement of magmatic plutons at different structural levels, from the ductile lower crust to the brittle upper crust. In this framework, the migration of fluids is favored by the kinematics of the shear zones, since the intermediate shear axis plays a significant role in defining the orientation of the structural channels where permeability is promoted (e.g. Sibson, 2000; Rowland and Sibson, 2004; Liotta and Brogi, 2020). In particular, shear zones with a dominant transcurrent regime, such as transfer zones (Lister and Davis, 1989; Gibbs, 1990), due to their geometrical and kinematic features, can develop into relatively delimited permeable crustal volumes where magmas can be channeled, and feed shallow-level plutonic bodies, that rapidly cool down during exhumation. It is generally believed that this fast exhumation is accompanied by brittle deformation during cooling of the magmatic body (e.g. Moyen et al., 2003; Liu et al., 2020). However, our analysis of the syn-tectonic Porto Azzurro pluton (Elba Island, Fig. 1) shows that its exhumation is accompanied by localized ductile shear zones, developing along magmatic dykes and hydrothermal veins, involved subsequently in brittle deformation. The recognized sequence of events implies particular relationships among exhumation, cooling, stress and strain localization. To unravel the interaction between the structural history and exhumation-driven cooling, an integrated approach of meso- and micro-structural studies, geochronology, thermochronology and rheological modeling is here successfully applied.

The inner zone of the Northern Apennines (Fig. 1) represents an ideal area for investigating the above described relationships, i.e. extensional structures, transfer zones (Liotta, 1991; Acocella and Funiciello, 2006;

* Corresponding author.
E-mail address: richard.spiess@unipd.it (R. Spiess).

https://doi.org/10.1016/j.jsg.2021.104326
Received 27 June 2020; Received in revised form 9 March 2021; Accepted 16 March 2021
Available online 23 March 2021

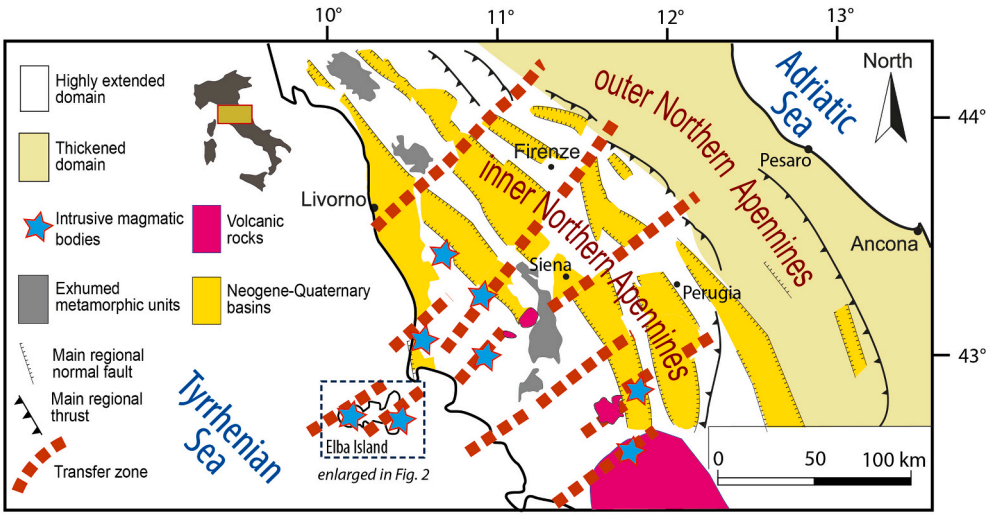

Fig. 1. Structural sketch map of Northern Tyrrhenian Basin and Northern Apennines. The main Pliocene–Quaternary basins, transfer zones and Neogene–Quaternary intrusive bodies are indicated (after Dini et al., 2008).

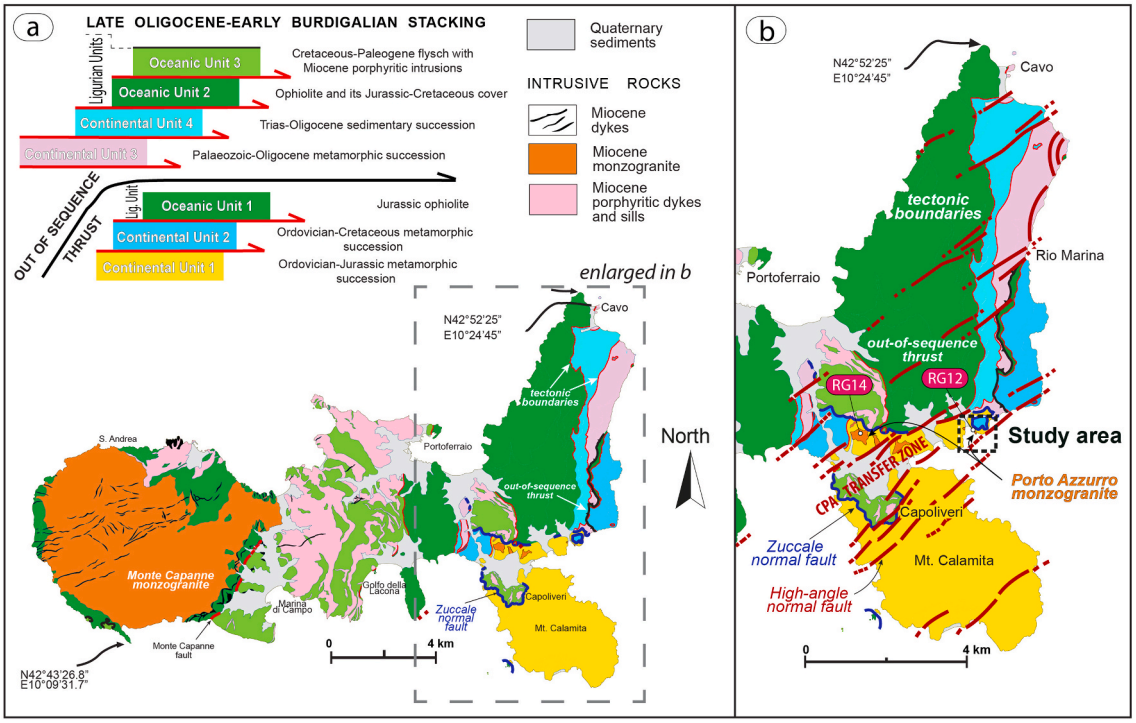

Fig. 2. Geological sketch map of Elba Island. The main faults, the study area and the location of the dated ($^{206}Pb/^{238}U$ in zircon) samples (RG12 and RG14) are indicated.

Dini et al., 2008; Liotta and Brogi, 2020) and emplacement and exhumation of magmatic bodies (Westerman et al., 2004; Dini et al., 2005, 2008) in a thinned continental crust (22–24 km, Di Stefano et al., 2011, with references therein). This area, in fact, is affected by extensional tectonics since early-middle Miocene (Carmignani et al., 1995), after having experienced thickening during the Tertiary Alpine orogenesis (Carmignani et al., 2001; Molli, 2008; Rossetti et al., 2015; Bianco et al., 2019).

The methodological approach we applied is based on the integration of: (a) field-mapping at different scales, in order to frame the (i) geometrical relationships between granitic pluton and hosting rocks, and (ii) fracture network, discrete shear zones, kinematics and cross-cutting relationships; (b) micro-structural studies aided by EBSD, to define the deformation temperatures on selected samples from ductile shear zones; (c) geochronological and thermochronological analyses plus rheological modeling, to define the timing of deformational events during exhumation.

2. Geological setting

Elba (Figs. 1 and 2) is part of the inner zone of the Northern Apennines, an Alpine belt deriving from the convergence and collision (Cretaceous-early Miocene) between Adria (a microplate, belonging to the Africa plate) and the Sardinia-Corsica Massif of European pertinence (Molli, 2008 for a review; Handy et al., 2010). Collision determined the stacking of oceanic and continental tectonic units deriving from the

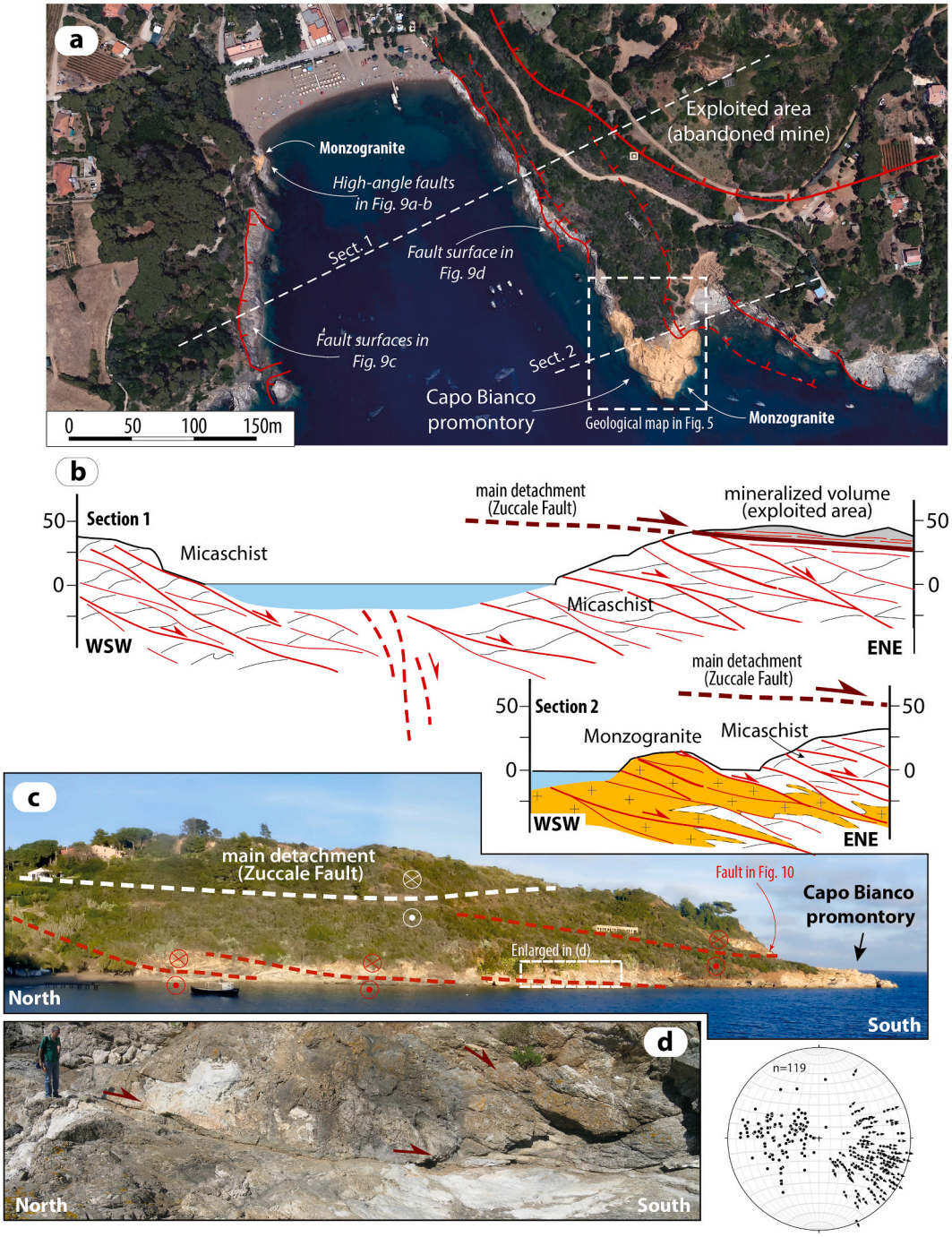

Fig. 3. a) Google Earth photograph of the Barbarossa bay where the analyzed monzogranite is exposed; the main structural elements and the mineralized volume corresponding to the Zuccale Fault is also indicated; b) geological sections across the bay with the main structural elements; c) panoramic view of the eastern side of the bay with the main faults and the analyzed monzogranite; d) detail of an extensional detachment fault accompanying the deformation in the footwall of the Zuccale Fault; the stereographic diagram (lower hemisphere, equiareal projection) illustrates the poles of the minor faults linked to the detachments and their kinematics.

palaeo-geographic domains of the Northern Apennines (Carmignani et al., 1994; Bianco et al., 2015). Since early-middle Miocene, inner Northern Apennines is affected by eastwards migrating extensional tectonics that consists in two main events (Brogi and Liotta, 2008; Barchi, 2010): (a) the first (early to late Miocene), characterized by an extension of at least 120% (Carmignani et al., 1994; Dallmeyer, and Liotta, 1998; Brogi, 2006; Brogi and Liotta, 2008), gave rise to low-angle normal faults; this event produced the lateral segmentation of the previously stacked tectonic units and the exhumation of mid-crustal rocks (Dallmeyer and Liotta, 1998; Brogi, 2008); (b) the second (Pliocene to Present) is defined by high-angle normal faults, that crosscut the previous structures (Liotta et al., 2010), and determined tectonic depressions where Pliocene to Quaternary continental and marine sediments deposited (Martini and Sagri, 1993; Pascucci et al., 2007; Brogi, 2011). The amount of extension related to these faults is estimated in about 6–7% (Carmignani et al., 1994). The opening of the Tyrrhenian basin (Bartole, 1995; le Breton et al., 2017) and the present crustal and lithospheric thicknesses, (22–24 and 30–50 km, respectively, Calcagnile and Panza, 19811; Locardi and Nicolich, 1992; Di Stefano et al., 2011), are the clearest evidence of the extensional evolution.

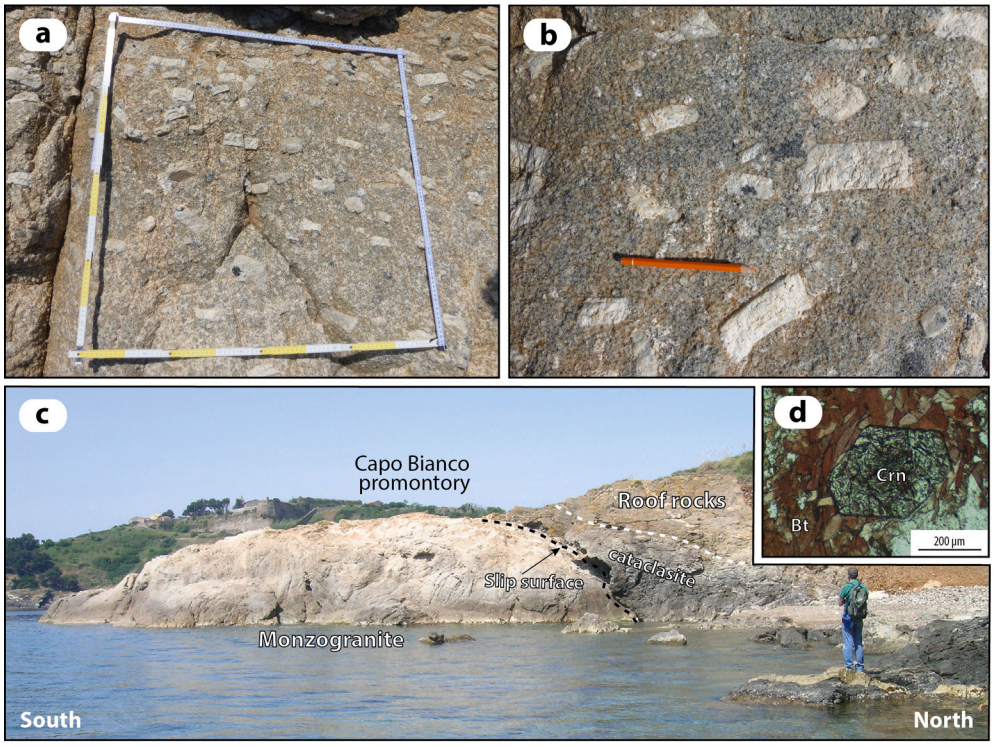

Fig. 4. a) Aligned K-feldspar megacrysts defining the magmatic foliation of the monzogranite; b) details of K-feldspar megacrysts; c) panoramic view of the Capo Bianco promontory with the tectonic relations of the monzogranite and the hosting rocks; d) euhedral corundum growing within quartz-free, biotite-rich domain of the micaschist next to the monzogranite.

Since the Langhian, the migration of extension was accompanied by magmatism, mostly of hybrid mantle-crustal signature, with an eastward younging direction (Serri et al., 1993; Peccerillo, 2003). Thermal perturbations related to the emplacement into the upper crust of late Miocene-Pliocene plutons, such as the Porto Azzurro monzogranite (Fig. 2) at Elba (Westerman et al., 2004; Caggianelli et al., 2014), produced contact metamorphic aureoles (Rossetti et al., 2007; Zucchi et al., 2017; Caggianelli et al., 2018; Pandeli et al., 2018) and widespread epithermal and mesothermal mineralization through Tuscany and Elba (Dini, 2003) where ore deposits have been exploited for centuries. The emplacement of the Porto Azzurro Pluton is interpreted as controlled by the activity of the Capoliveri-Porto Azzurro (CPA) transfer zone (Liotta et al., 2015), affecting the southern part of Elba (Fig. 2).

Exhumation of Elba's magmatic bodies was activated in part by fault activity (Westerman et al., 2008): among these, one of the most representative is the Zuccale extensional detachment fault zone (Keller and Pially, 1990), well exposed at Punta Zuccale (Fig. 2), juxtaposing the Ligurian Units upon the early–middle Triassic quartzite (Quarziti di Barabarca Fm., in Garfagnoli et al., 2005). The boundary is marked by a flat-lying mineralized extensional shear zone, up to 5 m thick and with a top-to-the-east sense of shear, regionally dipping to the East (Pertusati et al., 1993; Collettini and Holdsworth, 2004; Liotta et al., 2015). Our study area is located in the footwall of the Zuccale detachment, a few tens of meters below the main slip zone (Fig. 3).

The Porto Azzurro pluton is a coarse-grained monzogranitic body with K-feldspar megacrysts (Fig. 4), poorly exposed in eastern Elba. The best outcrops are located at Capo Bianco (Marinelli, 1959), flanking the Barbarossa bay (Fig. 5). The dimensions of this pluton are unknown, although gravity data (Milano et al., 2019) suggest an elliptical shape within the CPA transfer zone (Liotta et al., 2015) and revealing an intrusion even larger than the Monte Capanne pluton (Fig. 6), widely exposed in western Elba (Fig. 2) with diameter of c. 10 km and thickness of c. 2.5 km (Farina et al., 2010).

The age of the Porto Azzurro monzogranite is poorly constrained. Gagnevin et al. (2011) provided in-situ U–Pb zircon data for three grains yielding a weighted $^{206}Pb/^{238}U$ age of 6.53 ± 0.39 Ma. $A^{40}Ar$-^{39}Ar biotite date of 5.9 ± 0.2 Ma was obtained by Maineri et al. (2003). Magma emplacement took place at pressures of 200 - 175 MPa, as determined from mineral assemblages in the contact aureole (Duranti et al., 1992; Caggianelli et al., 2018). During magma cooling hydrothermal deposits of Fe-oxides and Fe-hydroxides formed at 5.53 ± 0.14 Ma (Wu et al., 2019). The wall and roof rocks (largely exposed in the Mt. Calamita promontory, Fig. 2) are the structurally deepest outcropping rocks of Elba (Porto Azzurro Fm., in: Garfagnoli et al., 2005). These are mainly represented by micaschist, quartzitic phyllite, quartzite and minor amphibolite levels (Barberi et al., 1967; Garfagnoli et al., 2005). In the whole Mt. Calamita Promontory, and especially in the Barbarossa bay, the micaschist and the monzogranite itself are injected by leucogranite dykes, quartz and tourmaline veins (Fig. 7), dissected by later faults (Dini et al., 2002, 2008; Musumeci et al., 2011; Viti et al., 2016; Zucchi et al., 2017).

3. Dataset

We present the collected dataset according to the planned methodological approach, finalized to reconstruct the deformation and exhumation history of the pluton. In the Capo Bianco area (Fig. 5), the monzogranite and its hosting rocks are structurally located in the footwall of the Zuccale extensional detachment. The hosting rocks are micaschist and quarzite (see Spina et al., 2019 for information on the protolith), with a well-developed schistosity, generally dipping gently westward to north-westward. Thisschistosity is defined by low-P parageneses, generated during contact metamorphism, up to muscovite-out conditions (Garfagnoli et al., 2005; Zucchi et al., 2017; Papeschi et al., 2017; Caggianelli et al., 2018) producing K-feldspar + andalusite and, in quartz-free domains, K-feldspar + corundum (Fig. 4d). For the sake of clarity, the data are presented in distinct sections, starting with the petrographical description of the monzogranite.

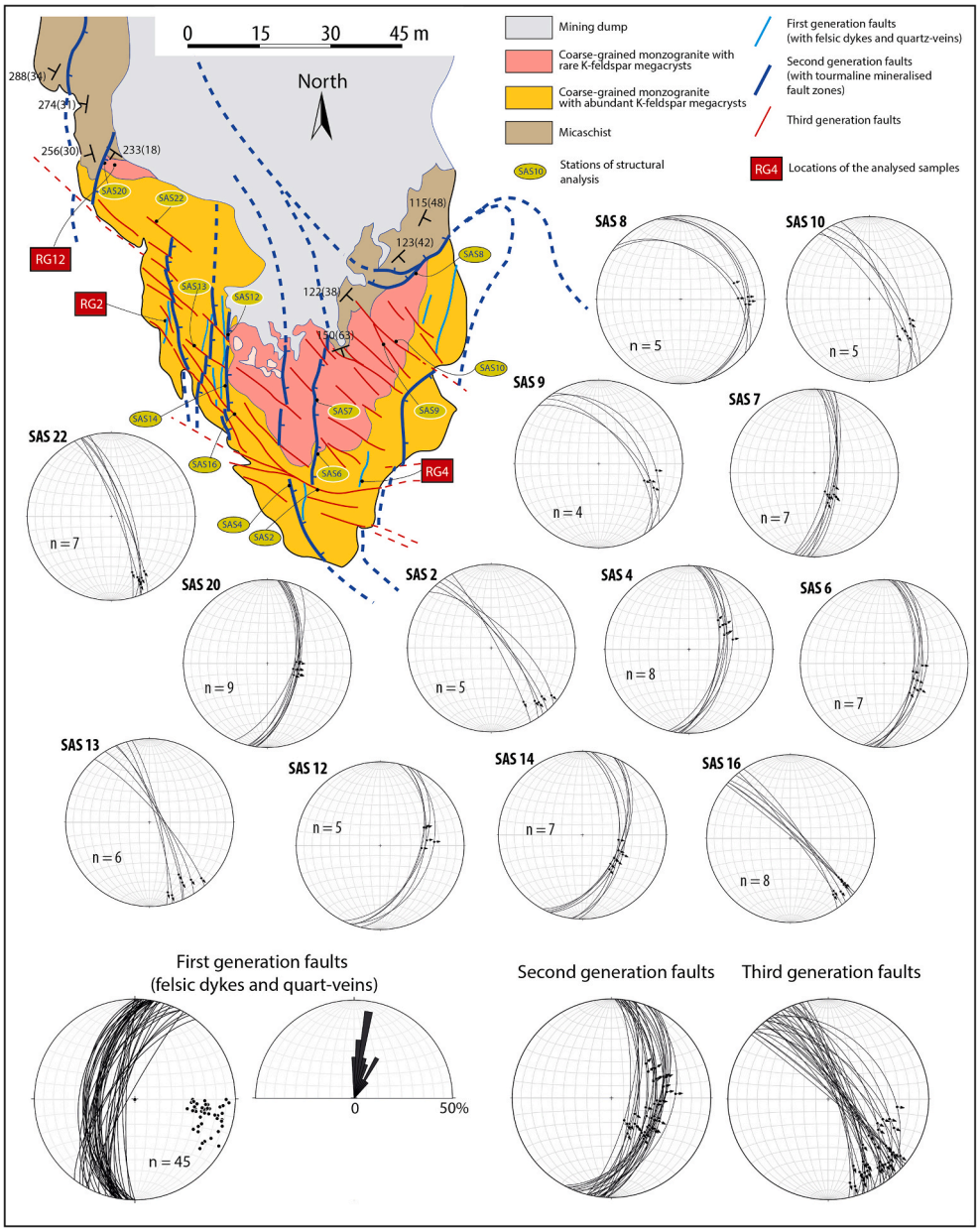

Fig. 5. Geological map of the Capo Bianco promontory. Stations of structural analyses and relative data are reported in stereographic diagrams (lower hemisphere, equiareal projection). The location of the analyzed samples for microstructural analyses is also indicated. Structural and kinematic data of each fault generation, as described in the text, are reported in stereographic and rose diagrams (lower emisphere, equiareal projection).

3.1. Petrography of the monzogranite and felsic dykes

The texture of monzogranite is characterized by a coarse grain size, heterogeneous for the presence of K-feldspar megacrysts up to 10 cm in length. The mineral composition includes plagioclase, K-feldspar, quartz, biotite and minor white mica. Accessory phases are tourmaline, ilmenite, zircon, monazite, xenotime and apatite. K-feldspar frequently shows Carlsbad twinning and perthitic exsolutions (Fig. 8a) while plagioclase sometimes displays Albite-Carlsbad twinning and oscillatory zoning (Fig. 8b), reflecting the relatively fast magma cooling. Quantitative SEM/EDS analyses (Appendix: Table A1 and A2) indicate that plagioclase is generally zoned with andesine cores (X_{An} up to 0.39) and oligoclase rims (X_{An} down to 0.13). Biotite shows a marked pleochroism with a dark brown tone and the composition is characterized by an average Fe/(Fe + Mg) ratio of 0.56. Biotite frequently includes apatite, monazite and zircon, the latter two being surrounded by sharp metamictic halos (Fig. 8c). Quartz - K-feldspar intergrowths, display micrographic texture, reflecting last melt crystallization (Fig. 8d). Tourmaline is mostly of post-magmatic origin, being found in veins or along thin branched fractures. The possible former presence of cordierite (Marinelli, 1959) is revealed by the presence of clots made up of sericite and chlorite.

The felsic dykes, intruding the monzogranite and wall rocks, are medium- to fine-grained, and heterogeneous for the presence of larger K-feldspars, up to 5 mm in length. The mineral composition includes K-feldspar, plagioclase (X_{An} = 0.14–0.16), quartz, tourmaline ± biotite ± white mica ± cordierite, with accessory phases represented by ilmenite, apatite, zircon and monazite. Thus, felsic dykes can be classified as tourmaline leuco-monzogranite. K-feldspar displays Carlsbad twinning and perthitic exsolutions. Plagioclase is present in minor amounts with respect to monzogranite and albite polysynthetic twinning is barely visible. Tourmaline is generally more abundant in the felsic dykes

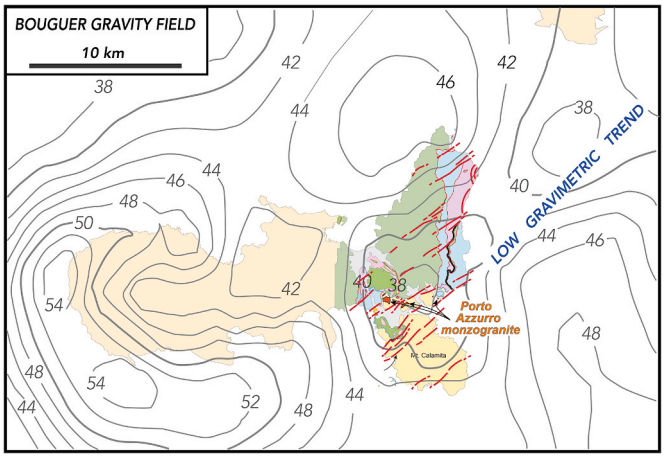

Fig. 6. Bouguer gravity field after Milano et al. (2019). Isolines are in mGal. NE-trending faults are matching the low gravimetric trend, that is here related to a regional transfer zone where magmatic bodies emplaced.

compared to the monzogranite. SEM/EDS analyses reveal that the tourmaline can be classified as Schörl. SEM analyses on rare biotite crystals reveal an elevated content in Fe with an average Fe/(Fe + Mg) of 0.74, distinctly higher than the value found in biotite of the monzogranite. White mica ± chlorite occur as a common product of alteration at the expense of biotite, felspars and cordierite. Late magmatic muscovite is very rare. Analysis of zircon in one sample revealed an extremely high concentration of U (UO_2 up to 5.68 wt%) that can be ascribed to disequilibrium partitioning of U between crystal and melt (Wang et al., 2011).

The preferred orientation of the euhedral K-feldspar megacrysts in monzogranite, well visible in the field (Fig. 4) and related to melt-present conditions (Paterson and Newton, 1989), is barely recognizable at the scale of the optical microscope. In the felsic dykes, however, it can be easily recognized, even though the K-feldspars are rarely euhedral, owing to subsolidus deformation.

3.2. Structural features

Micaschist and monzogranite are deformed by 3 discrete faulting episodes (Fig. 5). Tourmaline is present in the damage zone and along the slip-surface of the first two generations of faults, thus suggesting their development in a short time interval, in the frame of a progressive deformation. The faults of the last episode are without hydrothermal mineralization in their damage zones.

The first generation of sub-vertical faults, N–S and NNE-striking, crossed the monzogranite, the related dykes and hosting rocks.

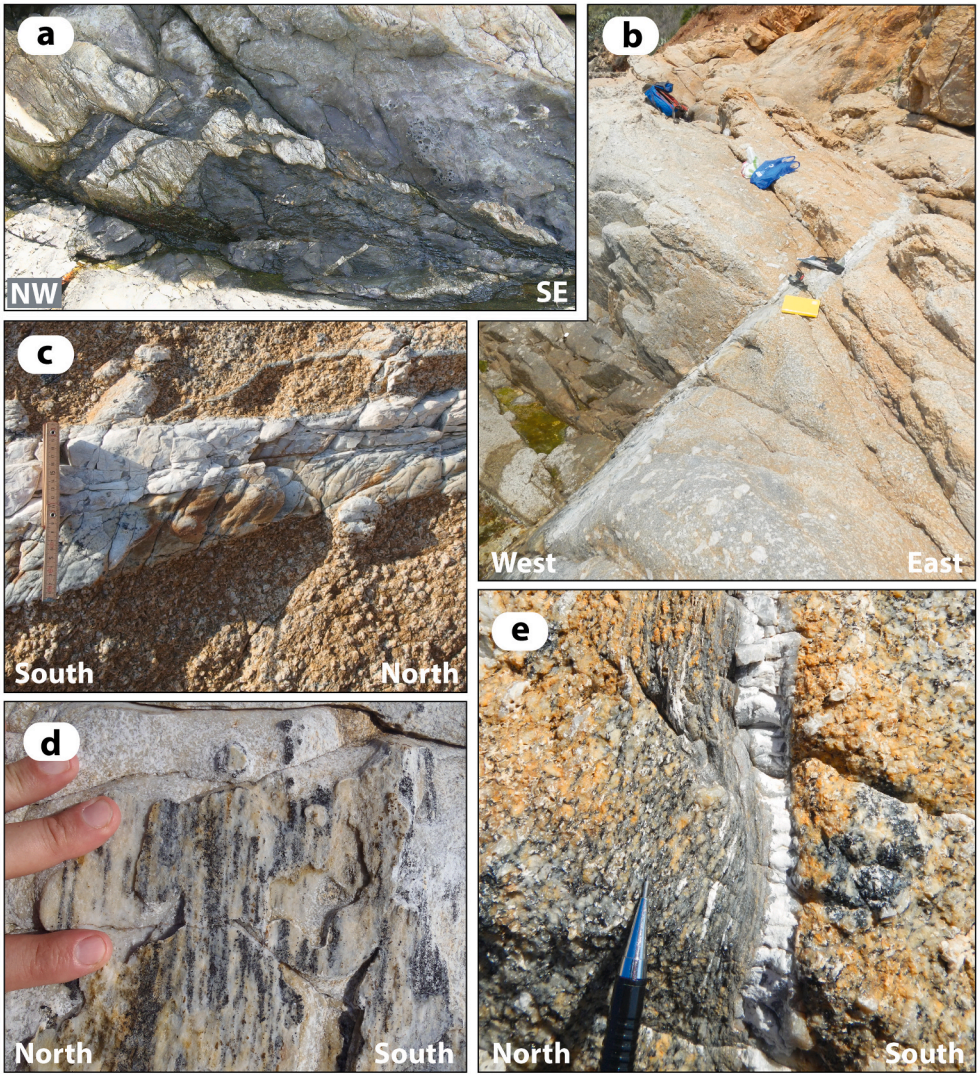

Fig. 7. a) dm-thick felsic dykes intruded within micaschist affected by second generation extensional faults; b) felsic dyke intruded within the monzogranite sampled for microstructural analyses (sample RG2); c) detail of the felsic dyke analyzed with EBSD, illustrating the internal foliation and S–C fabric; d) L-tectonite consisting of tourmaline lineation developed on the felsic dyke-surface foliation; e) hydrothermal quartz-rich vein and the mylonitic foliation affecting the adjacent monzogranite.

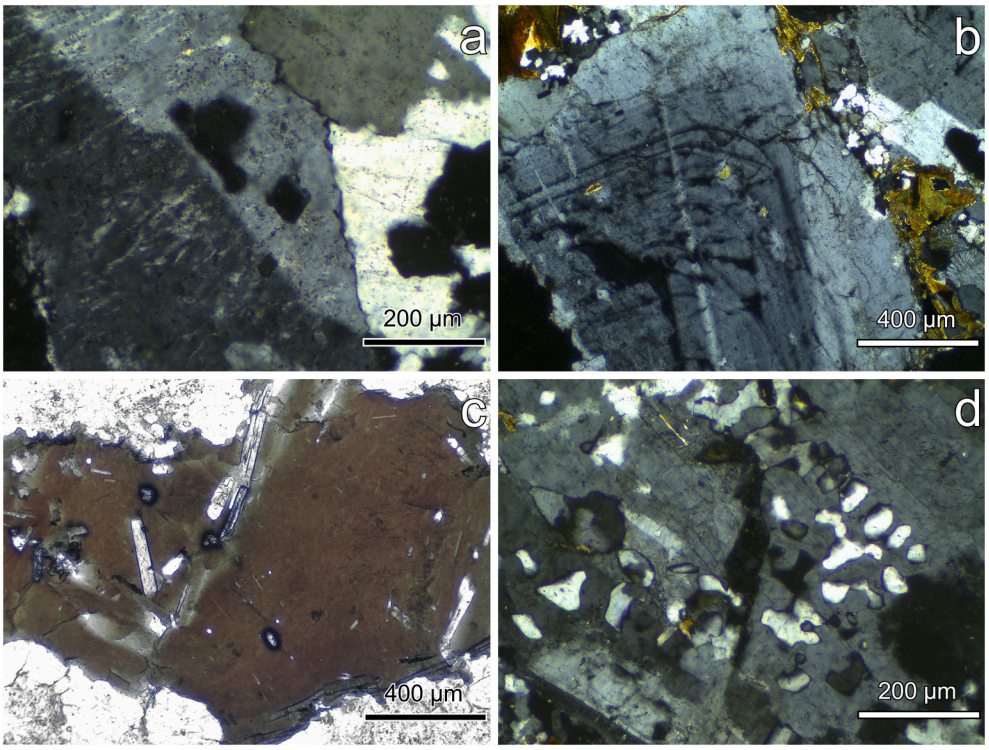

Fig. 8. Micrographs of petrographic features of the Porto Azzurro monzogranite in plane polarized (PPL) and crossed polars (CP) light. a) Karlsbad twinned K-feldspar with perthitic exsolution lamellae; b) plagioclase with oscillatory zoning (CP image); c) basal section of biotite including elongated apatites and tiny zircon and monazite crystals surrounded by metamictic halos (PPL image); d) K-feldspar-Quartz granophyric intergrowth (CP image).

Magmatic melt was channeled along these faults, resulting in decimeters-thick tourmaline-rich felsic dykes. Within these dykes, a pervasive foliation, parallel to the contact with the hosting rocks, is recognizable (Fig. 7). Tourmaline lineation, formed during shearing along the mylonitic foliation, is more evident close to the boundary between the dykes and the hosting monzogranite (Fig. 7d). Finally, cm-thick quartz-rich veins postdated the felsic dykes (Fig. 7e).

The second generation of faults consists of sub vertical NE-trending, left-lateral oblique-slip faults exposed in the western part of the Barbarossa bay (Fig. 9a and b) and of sub-horizontal to gently E-dipping normal faults (Fig. 9c). Both types of faults dissect all previous structures and are characterized by tourmaline in their shear zones and by offsets ranging from few to tens of meters (Fig. 3).

The left-lateral oblique-slip faults are interpreted as minor faults associated to the CPA transfer zone (Fig. 2). The low-angle normal faults are subsidiary structures of the Zuccale normal fault (Fig. 3), affecting its footwall (Liotta et al., 2015).

Low-angle normal faults are characterized by the presence of up to 30 cm thick mineralized cataclasite: tourmaline mineralization occurs in the monzogranite (Fig. 9d), whereas graphite and tourmaline are typically present in micaschist (Fig. 9e). Dilatational shear veins filled by tourmaline and subsequent Fe-oxides and/or Fe-hydroxides typify the damage zone of these latter structures. Kinematic indicators are given by the relationships between the tourmaline and/or graphite-bearing fault zones and associated minor structures, and by mesostructures on the fault-slip plane. These latter are represented by lunate structures, grooves, mega-grooves, slickenlines, quartz-fiber steps, with a top-to-the-east sense of shear, defining a clear normal movement, consistent with the kinematics of the Zuccale normal fault (Pertusati et al., 1993; Keller and Pialli, 1990; Collettini and Holdsworth, 2004).

A significant low-angle normal fault characterizes the Capo Bianco promontory, and affects the roof of the monzogranite (Fig. 10a and b). It defines a more than 3 m thick cataclasite level, mostly made up of comminuted micaschist and monzogranite, mineralized by tourmaline and Fe-oxides and/or Fe-hydroxides. Along the main slip surface a mm-thick shear vein, made up of Fe-oxides and/or Fe-hydroxides is recognizable. Along this slip surface a cm-thick felsic dykelet, parallel to the shearing plane, is also hosted (Fig. 10c). Furthermore, a similar dykelet is deformed in the cataclasite (Fig. 10d), indicating fault activity during dyke injection. Kinematic indicators are consistent with the Zuccale detachment (Fig. 10a).

The occurrence of tourmaline and quartz in both NE-striking left-lateral oblique-slip faults and low-angle normal faults, as well as the deposition of graphite within the cataclasite, indicates that both fault systems were coeval with mineralization. The comminution of both tourmaline and quartz within the fault zones, strongly suggests that the activity of both sub-vertical and sub-horizontal faults continued after the mineralization event, too.

The third generation of faults is mostly made of NW-striking sub-vertical structures. These faults show up to 50 cm thick damage zones with shear fractures and minor faults. The cataclasite is composed of comminuted rock elements, ranging in size from 0.1 to 3 cm. The angular relationships between minor fractures and the main slip surfaces, together with extensional jogs (Fig. 11c), indicate a dominant right-lateral shear component (Fig. 11a and b). Slickenlines on fault planes are oblique, with pitches ranging from 120° to 140° (Fig. 11d and e).

3.3. Microstructural analysis

Rock samples from each structural setting were studied microstructurally. These include felsic dykes and quartz-rich hydrothermal veins, as well as the monzogranite they intruded along the first fault generation, where ductile deformation concentrated. We present EBSD data of two key samples to highlight microstructural features representative of the distinct deformation conditions.

The first sample (Fig. 7c, sample RG2) consists of a foliated felsic dyke with a maximum thickness of c. 20 cm, crosscutting the

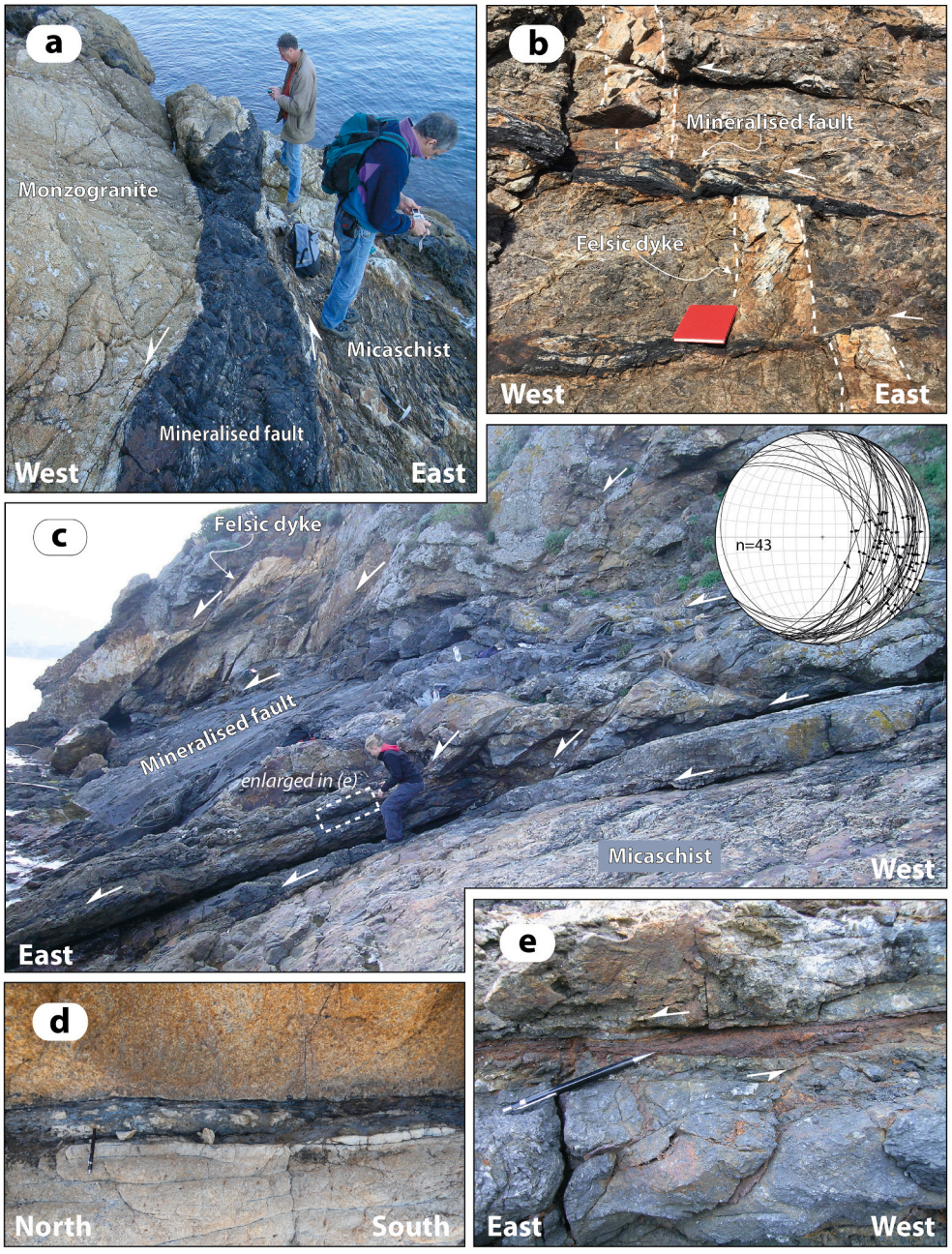

Fig. 9. Photographs illustrating details of the second generation faults in the Barbarossa bay and Capo Bianco promontory: a) meter-thick tourmaline-rich mineralized fault at the boundary between the monzogranite and the host rocks; b) shear veins parallel to cm-thick fault zones mineralized by quartz and tourmaline, dissecting a dm-thick felsic dyke; c) panoramic view of the low-angle normal faults characterizing the footwall of the Zuccale Fault; d) detail of a fault zone mineralized by tourmaline and quartz characterizing the footwall of the Zuccale Fault and affecting the monzogranite; e) detail of a fault zone mineralized by Fe-oxyhydroxides characterizing the footwall of the Zuccale Fault and affecting the micaschist in the fault system shown in (c).

monzogranite. The dyke shows a clear mylonitic fabric with evidence of dextral extensional shear, resulting in strongly boudinaged K-feldspar (Kfs). In Fig. 12a, a boudinaged Kfs-clast with recrystallized necks and deformed tails, is enveloped by dynamically recrystallized 10–50 μm large quartz crystals. Plagioclase recrystallized to significantly smaller grains (<10 μm), that is interlayered between the Kfs clasts and the quartz tails.

EBSD analysis was applied on five areas of sample RG2 to document the deformation microstructures, as well as the type of crystallographic preferred orientations (CPOs). This approach provides an insight into the activated slip systems within quartz and Kfs during plastic deformation, and allows to estimate the deformation temperatures.

Fig. 12a shows that boudinaged Kfs clasts are twinned according to the Carlsbad law, and the recrystallized grains within the neck have variable misorientations.

Four of the five selected sites for quartz CPO analysis are in the Kfs-rich parts of the dyke, whereas the fifth is located in a quartz-dominated vein containing boudinaged tourmaline and few strongly deformed Kfs crystals. Fig. 12b reveals that most of the recrystallized quartz grains have a reddish color and hence a strong attitude to have their c-axes aligned towards the observer. The crystallographic orientations of all quartz grains within the analyzed sites give identical indications.

Pryer (1993) suggests that Kfs plastic deformation is only expected at temperatures exceeding 600 °C. We have tried to reconstruct from the EBSD map the possible slip systems that may have operated during the ductile necking of the Kfs clast. For this purpose, we have constructed a pole figure plot that considers just one analytical point for every recrystallized Kfs-grain in the neck (Fig. 13). The most likely operating slip system during Kfs boudinage was (110)1/2[1–12]. Dispersion of the slip directions in an ill-defined girdle may suggests dislocation creep to have been accommodated by grain boundary sliding and possibly by a diffusion controlled mass transfer process. The latter is suggested by the growth of Kfs-fringes in the strain shadow of the large grey undeformed plagioclase crystal (on the lower right of Fig. 12a), which must have

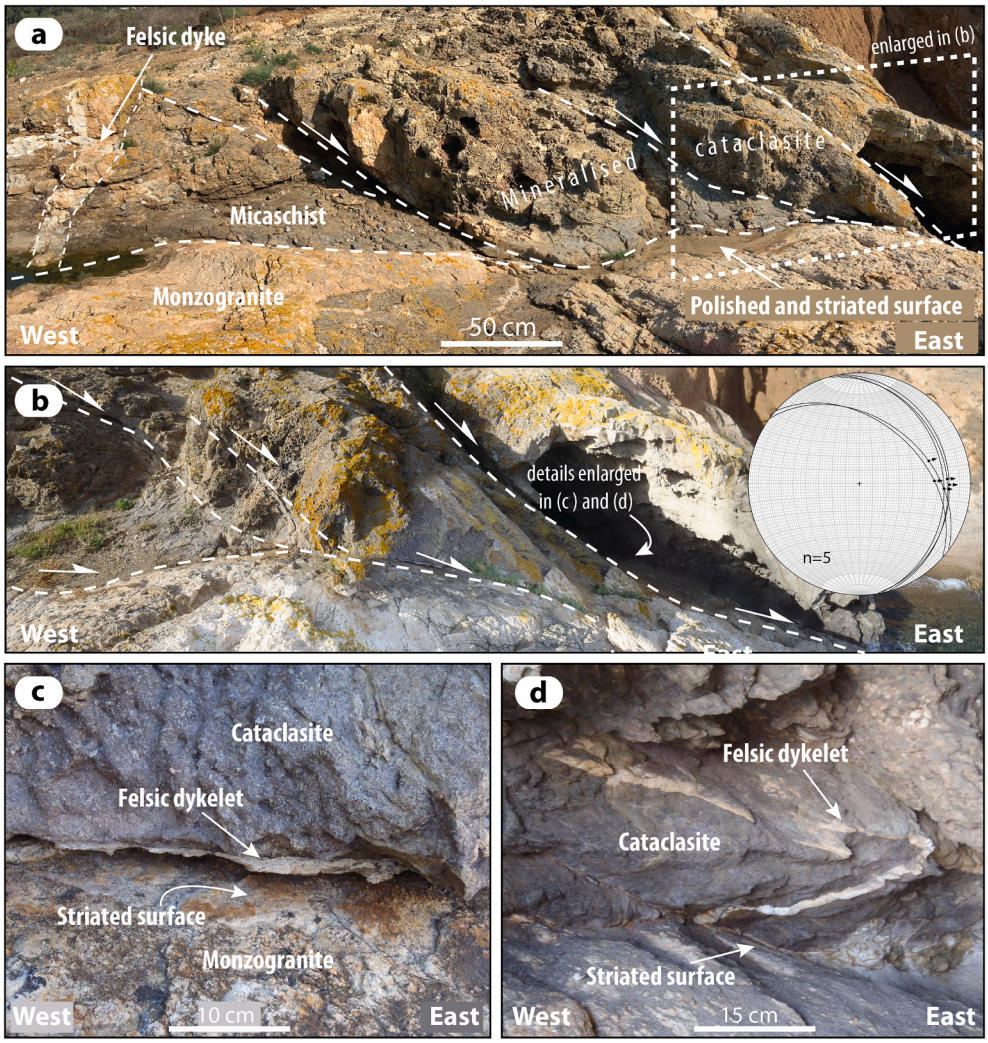

Fig. 10. Photographs illustrating second generation faults: a-b) panoramic view of the extensional fault system separating the monzogranite from the roof rocks (micaschist) characterizing the footwall of the Zuccale Fault in the Capo Bianco promontory; c) detail of a cm-thick felsic dykelet assisting deformation along the slip surface of the fault zone illustrated in (a) and (b); d) felsic dykelet injected in the cataclasite and ductilely deformed during faulting.

been in a hard slip position.

TEM analysis of experimentally deformed Kfs crystals (Willaime et al., 1979; Scandale et al., 1983) in the temperature range between 700 and 900 °C and at strain rates of 2×10^{-6}sec^{-1}, shows that the easiest slip systems in Kfs are those with glide along the cleavage planes (010)[001] and (010)[101]. Another possible slip system is (110)1/2[1–12], coherent with our data.

Deformation temperatures consistent with 600 °C are also supported by the recrystallized quartz grains. This is confirmed by the pole figures shown in Fig. 13, where quartz c-axes maxima are concentrated in the central part, and poles to a-prisms {11–20} and m-prisms {10-10} are aligned along the primitive great circle. Schmid and Casey (1986) have shown that in metamorphic rocks deformed at normal geological strain rates, these quartz pole figures are characteristic of the upper amphibolite facies conditions, and are consistent with temperatures of about 600 °C, already suggested by the plastically deformed Kfs clasts.

Concerning the second sample (RG4), we have studied the transition between the foliated monzogranite and a tourmaline-bearing quartz-rich hydrothermal vein where an evolution from a mylonitic to ultramylonitic fabric is observed. Fig. 14a shows the areas analyzed in the scanned thin section (at plane polarized light) with a closely flat running foliation in the ultramylonitic zone (Fig. 14b). In the upper third of the thin section, larger biotite flakes highlight the foliated monzogranite. In the central mylonitic part, biotite has become strongly deformed and altered. We present data from two microstructurally distinct areas (red squares, in Fig. 14a and b), that progressively accommodate increasing amounts of deformation in the mylonitic part (Fig. 15a and b), which allow us to understand the deformation mechanisms and temperature conditions affecting this micro shear zone. The CPOs of these recrystallized quartz grains will then be compared with those of sample RG4, previously described and which deformed at about 600 °C.

Fig. 15a, an Inverse Pole Figure (IPF) color coded orientation map, shows how quartz of the foliated monzogranite deforms when it meets the upper shear zone boundary. Large grains of the quartz layer show only limited internal deformation in form of the arranged subgrain-boundaries (upper part of Fig. 15a). Grain size reduction is confined to high stress zones, distinguished by fracture propagation. Here, recrystallization results in a typical grain size smaller than 10 μm. The EBSD orientation map shows that recrystallized grains deriving from different quartz domains mix up and assume misorientations among grains from 2° to >60°. Mixing up of recrystallized quartz grains originally belonging to distinct large quartz grains suggest that grain boundary sliding has been important during this incipient deformation (Ishii et al., 2007).

In the central part of the mylonitic shear zone, grain size reduction of quartz is pronounced (Fig. 15b), even though few larger remnant grains, showing core-mantle microstructures, are still preserved. Plots of the EBSD data in pole figures (Fig. 13e) show a distribution of c-axes

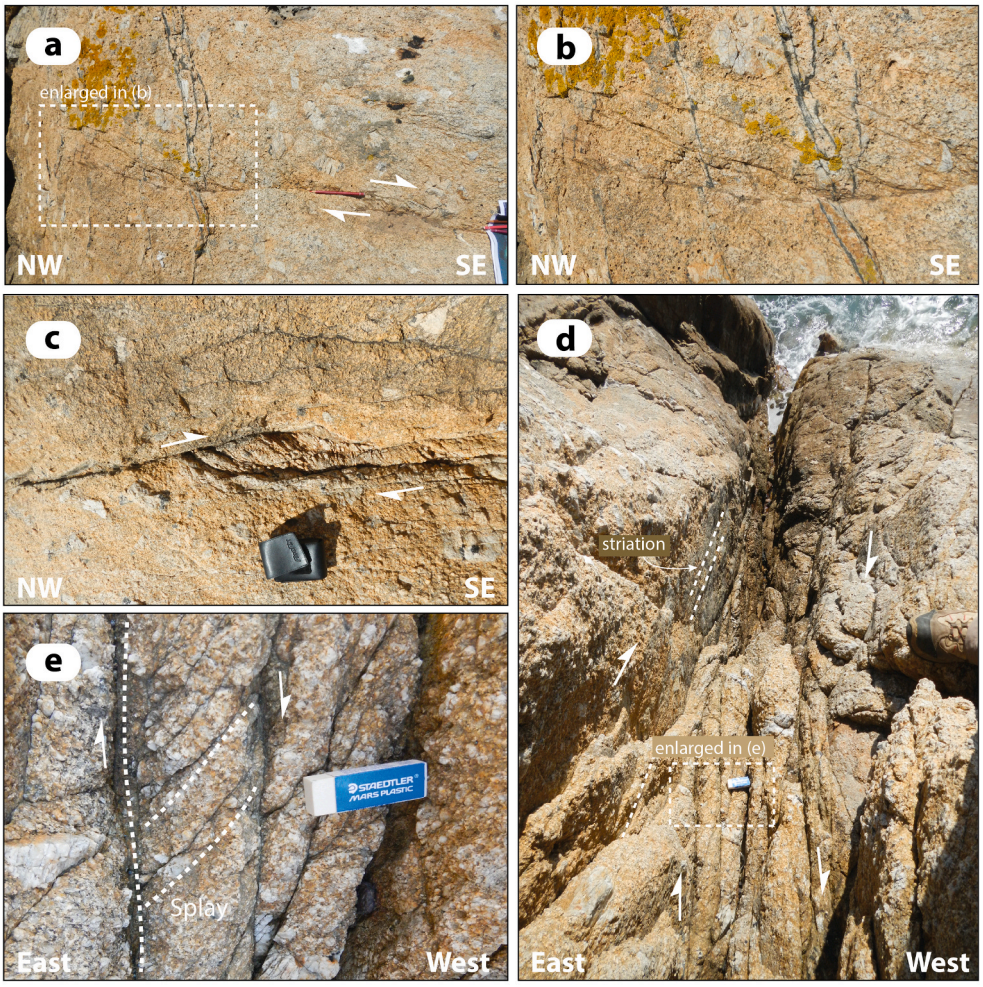

Fig. 11. Photographs illustrating details of the third generation faults affecting the monzogranite in the Capo Bianco promontory: a-b) horsetail fractures developed in the tip-damage zone of a right-lateral strike-slip fault; c) dm-sized extensional jog formed in the linking damage zone of two overstepping right-lateral strike-slip faults; d-e) detail of a right-lateral strike-slip fault zone and minor (i.e. splay) structures.

characteristic for a type-I crossed girdle according to Lister (1981), suggesting the activation of basal <a>, rhombs <a> and prism <a> slip systems, typically operating at greenschist facies conditions during metamorphism and therefore at temperatures of about 450 °C. The intense strain gradient that evolved within the shear zone, resulting in complete recrystallization and progressive grain size reduction towards the ultramylonitic part of the shear zone, suggests a strain softening mechanism. Considering that the analyzed shear zone nucleated on a tourmaline-bearing quartz-rich hydrothermal vein, it is reasonable that fluids conveyed along the vein promoting strain softening. Hence, ductile deformation of the veins and adjacent monzogranite clearly occurred later and at lower temperature than the deformation affecting the felsic dykes.

3.4. U–Pb geochronological data

After having defined deformation characteristics and their related temperatures, we now focus on the time constraints by U–Pb geochronological data. Since we consider existing U–Pb SIMS analyses on only three magmatic zircon grains from the Porto Azzurro monzogranite (Gagnevin et al., 2011) not robust enough from a statistical point of view, we decided to analyze 79 out of 132 inspected zircon grains from two samples of the monzogranite exposed in Capo Bianco promontory and La Serra locality (Fig. 2). We have analyzed them with LA-ICP-MS for U–Pb zircon dating (see appendix).

U–Pb data were obtained for sample RG14 from the La Serra locality and sample RG12 from the Capo Bianco locality (Table A3).

Sixty-one zircon grains were initially studied from RG14 using cathodoluminescence (CL) imaging in the SEM. Zircon grains are characterized by complex internal features, with rare continuous oscillatory zoning (Fig. 16a). Instead, zircon grains show usually domains or well-defined cores characterized by different CL features with respect to the surrounding rims or rim-domains (Fig. 16a–d). Brighter irregular surfaces can occur between these different domains (Fig. 16c and d).

Thirty-nine U–Pb analyses were performed on thirty-eight selected zircon grains. Spot analyses were located mainly at the outer rims with oscillatory zoning. U–Pb results are mostly discordant with only seven concordant data. $^{206}Pb/^{238}U$ apparent ages range from 5.6 to 7.2 Ma.

Seventy-two zircon grains were inspected for sample RG12 at the SEM for internal features. The images revealed that zircon grains are commonly characterized by two domains with different CL features, locally separated by a brighter thin domain (Fig. 16e). Oscillatory zoning is common for the external domains (Fig. 16e), whereas the inner portions are characterized by more complex zoning features (Fig. 16f–h). Convoluted zoning is common and can locally interest entire grains (Fig. 16f and g), whereas sector zoning is less frequent but occupies large portions of the zircon grains (Fig. 16h).

Forty U–Pb analyses were performed on thirty-nine selected zircon grains. Spot analyses were located mainly at the outer rims with oscillatory zoning. U–Pb results are mostly discordant with only four

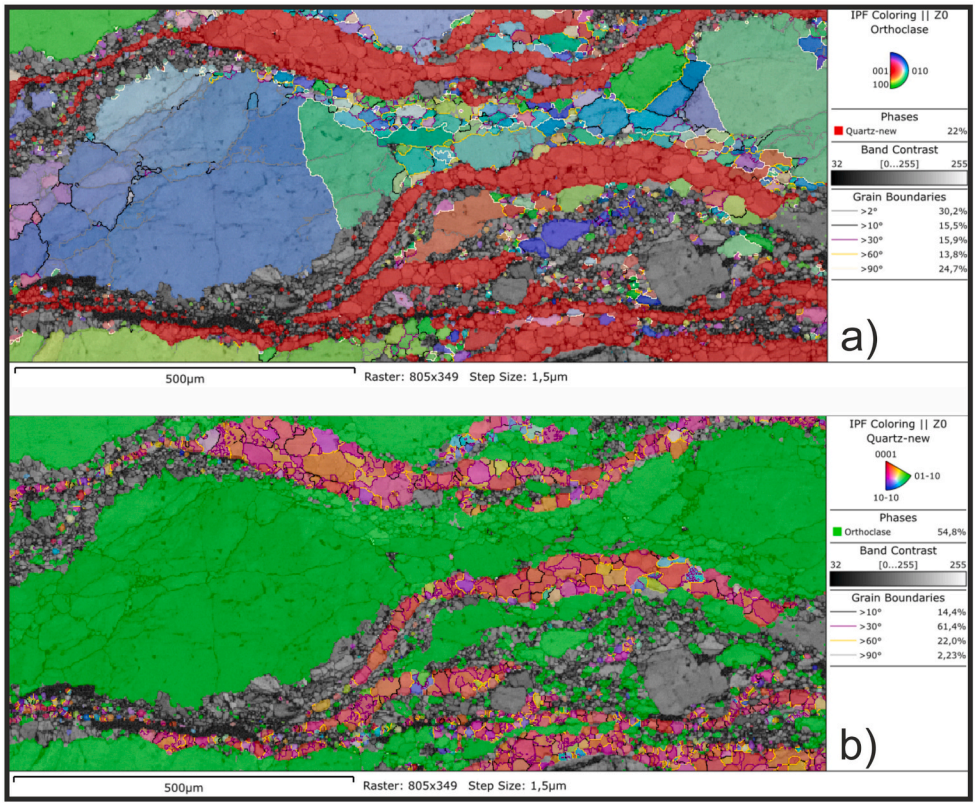

Fig. 12. EBSD misorientation maps of sample RG2. a) Kfs shown with IPF color coding, quartz distinguished as phase (red) and plagioclase shown in band contrast mode (grey tones). Boudinaged Kfs recrystallizes to new grains in the neck, showing crystallographic mismatches between 10 and >90°; b) anastomosing recrystallized quartz bands (IPF color coded) show a large preference for reddish colors, proving that the c-axis distribution of recrystallized grains is oriented towards the observer. Maximum of crystallographic mismatches along grain boundaries is > 30°. (For interpretation of the references to color in this figure legend, the reader is referred to the Web version of this article.)

concordant data. $^{206}Pb/^{238}U$ apparent ages range from 5.9 to 7.9 Ma.

The isotopic data obtained from the two samples are predominantly discordant and the $^{206}Pb/^{238}U$ data define a main peak between 6 and 7 Ma. The large occurrence of discordant data can be due to limitations of the LA-ICP-MS technique, unable to detect low concentrations of ^{207}Pb in young zircon grains. Another possible cause of discordance can be due to the analyses of distinct domains. Zircon shows complex zoning features, clearly associated to different growth stages. Although the analyses were mainly located at the outermost rims, likely associated with the last growth stage, we obtained a large age interval.

Combining the U–Pb data with CL images, we observed that the oldest ages (see Fig. 16h) are commonly associated with zircon cores showing CL features that are different and discordant with those of the surrounding thin rims, having oscillatory zoning. This observation suggests the presence of xenocrysts and inherited grains, in agreement with Gagnevin et al. (2011). Thus, excluding outliers (5 on 39 and 8 on 40 data, from sample RG12 and RG14, respectively), the average ages of the two samples are 6.4 ± 0.4 Ma and 6.4 ± 0.3 Ma (Fig. 17), respectively and very close to the Gagnevin et al. (2011) results. A similar U–Pb geochronological result was obtained from the Calamita schists, affected by contact metamorphism (LA-ICP-MS data on one zircon rim, Musumeci et al., 2011).

4. Post-emplacement thermo-rheological evolution

In order to constrain the deformational evolution with time of the above analyzed meso- and micro-structures, we simulated thermal and rheological evolution of the Porto Azzurro pluton for 1 Ma after its emplacement, taking into account the thermo-chronological constraints provided by zircon U–Pb and biotite Ar–Ar dating. In the following, we present the thermal and rheological evolution both in terms of static and dynamic approaches, with the aim to highlight the contribution of extensional tectonics in favoring cooling and migration of the brittle/ductile transition towards shallower structural levels.

4.1. Thermal evolution

The early cooling history of the Porto Azzurro monzogranite has been firstly simulated in static conditions through a unidimensional thermal model (Caggianelli et al., 2018) by numerically solving the differential equation:

$$\frac{\partial T}{\partial t} = \frac{K}{\rho C_p}\left(\frac{\partial^2 T}{\partial z^2}\right) + \frac{A}{\rho C_p} \quad (1)$$

where T, t and z are temperature, time and depth, respectively; K, ρ, Cp and A are thermal conductivity, density, specific heat and radiogenic heat production, respectively (Table 1). Crust and lithosphere thicknesses are fixed at 28 and 56 km respectively, in agreement with the supposed condition in Tuscany during late Miocene (Caggianelli et al., 2014). The pluton was assigned a tabular shape with a thickness of 3 km and an initial temperature of 850 °C. The effect of latent heat released during magma crystallization was considered in the temperature interval of 850-650 °C (Table 1).

The results obtained by a program in Stella ® code are here proposed through a T-t diagram for the first 1 Myr after magma emplacement fixed at 6.4 Ma (Fig. 18). In the same diagram, it is presented a second cooling history, ongoing dynamically during pluton unroofing at an initial rate of 5 mm/yr, decreasing exponentially according to a decay constant (c) of c. 10^{-6} yr^{-1}, similarly to the model proposed for the Monte Capanne intrusion (Caggianelli et al., 2014), reducing in 1 Myr the crust and lithosphere thicknesses to c. 25 and 53 km, respectively. The second cooling history incorporates the effect of heat advection due to rock exhumation and thus the differential equation, to be solved numerically, becomes:

$$\frac{\partial T}{\partial t} = \frac{K}{\rho C_p}\left(\frac{\partial^2 T}{\partial z^2}\right) + \frac{A}{\rho C_p} - vz\frac{\partial T}{\partial z} \quad (2)$$

with

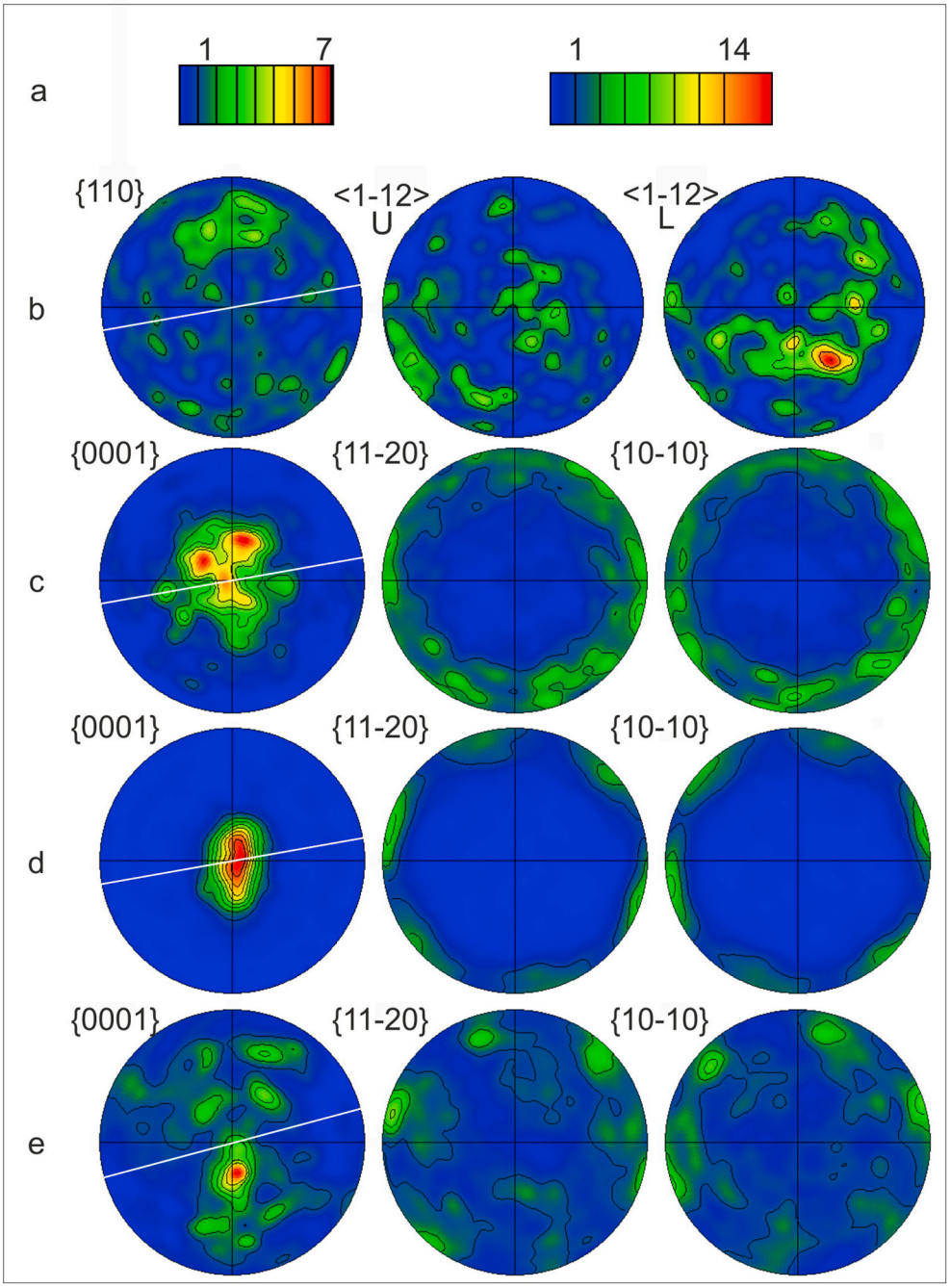

Fig. 13. Pole figures, equal area projections, lower hemisphere. a) Multiples of Mean Unit Densities expressed by color bars. Bar with maxima just above 7 belong to pole figures b, c,e, while bar with maximum at 14 belongs to pole figure d; b) pole figure of recrystallized grains in the neck of the boudinaged Kfs (Fig. 12a). White line is foliation trace. Maximum of {110} poles is consistent with this plane being the slip plain, while dispersion of slip direction <1-12> in a girdle centered on that maximum suggests that dislocation creep was accommodated by grain boundary sliding; c) quartz c-axis of grains within anastomosing bands within sample RG2 form a maximum in the central part of the pole figure, while poles to a- and m-prisms are dispersed along the equatorial section of the pole figure; d) distribution of c-axes within recrystallized quartz-rich band in sample RG2 forms a pronounced maximum in the center, while poles to a- and m-prisms form single maxima consistent with dextral shear and activation of prism <a> slip; e) quartz c-axis distribution within recrystallized grains of mylonitic monzogranite (sample RG4, Fig. 15b) forms a typical type-I crossed girdle, suggesting activation of basal <a>, rhomb <a> and prism <a> slip, and hence lower deformation T than for sample RG2. (For interpretation of the references to color in this figure legend, the reader is referred to the Web version of this article.)

$$v_z = \frac{dz}{dt} = -cz \tag{3}$$

A slight discrepancy between the two cooling histories is perceptible (Fig. 18), once about 0.7 Ma are elapsed from the time of emplacement, since the dynamical model reproduces a slightly faster cooling rate. The available dating of zircon by U–Pb and of biotite by Ar/Ar (see section 2) were plotted on the same T-t diagram. It is assumed that zircon age corresponds to crystallization at *c.* 800 °C, and that biotite age corresponds to a closure temperature of 430 °C, obtainable by Dodson (1973) formula with Ar diffusion parameters by Harrison et al. (1985). It may appear that the biotite closure temperature is too high with respect to the normally adopted values (e.g. 280–345 °C in Harrison et al., 1985), but the resulting number is mostly an effect of the size of the biotite laminae (width of 1–2 mm) and, above all, of the elevated cooling rate (at least 150 °C/Myr) expected for the top of the shallow Porto Azzurro magmatic body. Ar diffusion in biotite was recently simulated through numerical models by Skipton et al. (2018), which demonstrate that at 450 °C, Ar retention in biotite is sensibly controlled by the cooling rate. Anyway, modeled cooling histories are compatible with thermochronological data.

4.2. Rheological evolution

Numerical results of the cooling histories have been used to construct simplified rheological evolutions. For the estimation of the brittle strength we used the equation by Sibson (1974):

$$\sigma = \sigma_1 - \sigma_3 = \beta(1-\lambda)\rho g z \tag{4}$$

where σ is differential stress, β is a dimensionless parameter depending on the frictional coefficient and tectonic regime and λ is the pore fluid

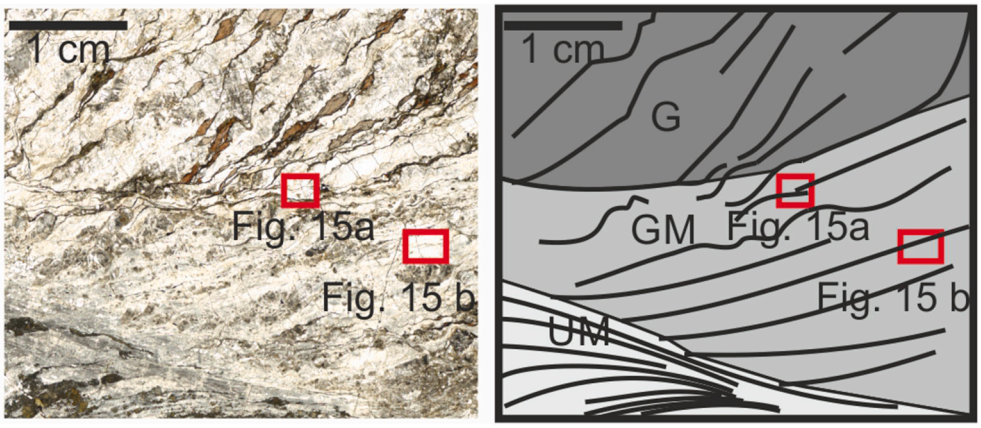

Fig. 14. Micrograph of a discrete shear zone localized within Sample RG4 and EBSD analysis areas. a) The foliated monzogranite (top) evolves to a mylonite in correspondence of EBSD analysis area Fig. 15a. There is a deformation gradient from mylonite towards ultramylonite next to the quartz-rich vein with green tourmaline clasts; b) sketch of Fig. 14a highlighting the different deformational domains: G = foliated monzogranite; GM = mylonite; UM = ultramylonite. Location of Fig. 15a and b is also shown. (For interpretation of the references to color in this figure legend, the reader is referred to the Web version of this article.)

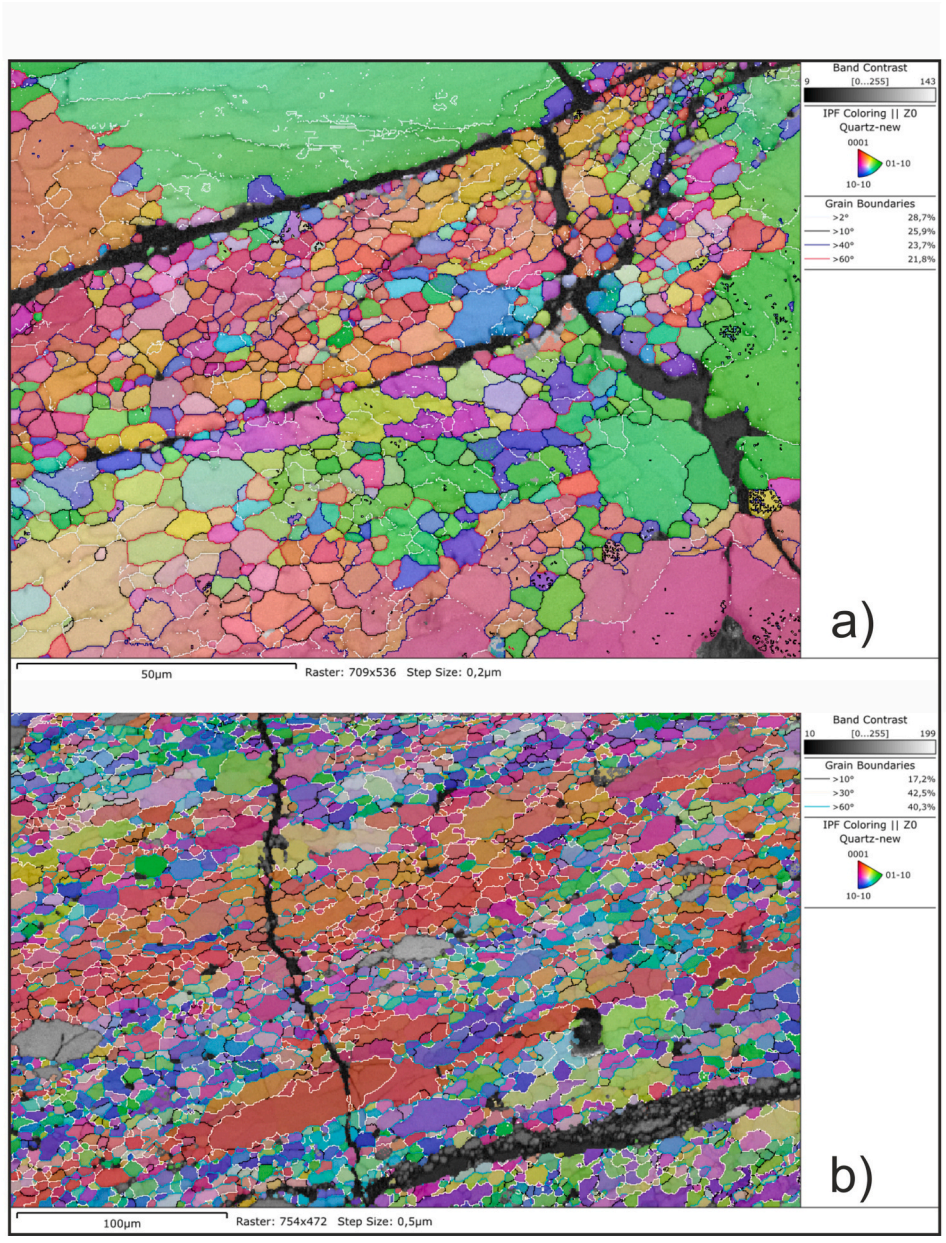

Fig. 15. EBSD misorientation maps (IPF color coding) of the areas indicated in Fig. 14 a) Monzogranite next to the mylonite boundary. Large quartz crystals are still preserved showing evidence of sub-grain boundaries. Recrystallization starts at sites of stress localization. Crystallographic mismatches are between 10 and > 60°. The small grain size and evidence for mixing up of recrystallized grains belonging to different quartz domains suggest grain-boundary sliding to have been important; b) monzogranite deformed at higher strain. Quartz is fully recrystallized and forms a mylonitic foliation trending ENE-WSW in the map. Some remnants of larger grains with core and mantle structure are still preserved. Maximum misorientation of adjacent grains is larger than 30°. Variegated colors of grains testify that slip occurred along multiple systems during mylonitic deformation. Non indexed grey phases are Kfs and plagioclase. (For interpretation of the references to color in this figure legend, the reader is referred to the Web version of this article.)

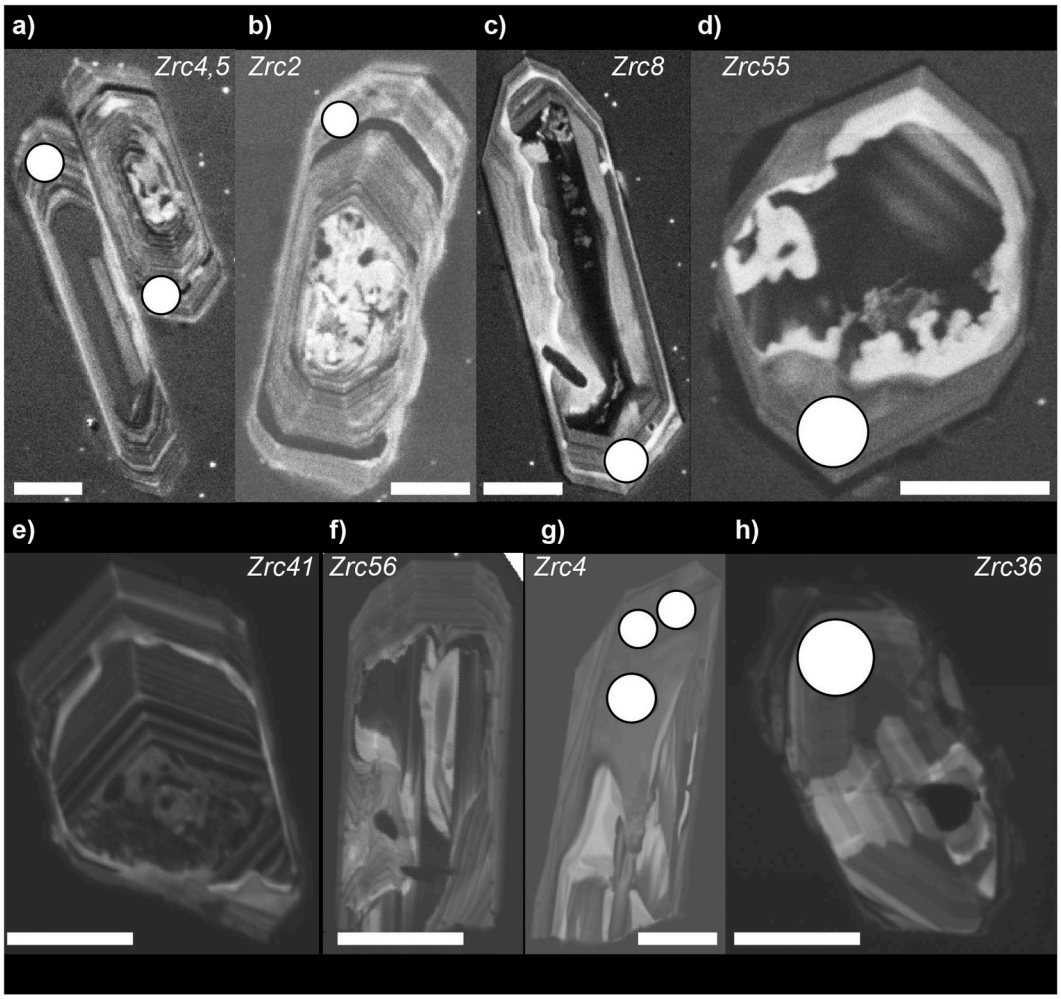

Fig. 16. Selected BSE-CL images of zircon grains from samples RG14 (a–d) and RG12 (e–h) representative of different CL features. Location of LA-ICP-MS spots is shown as well as Zrc#. Scale bar is 50 μm.

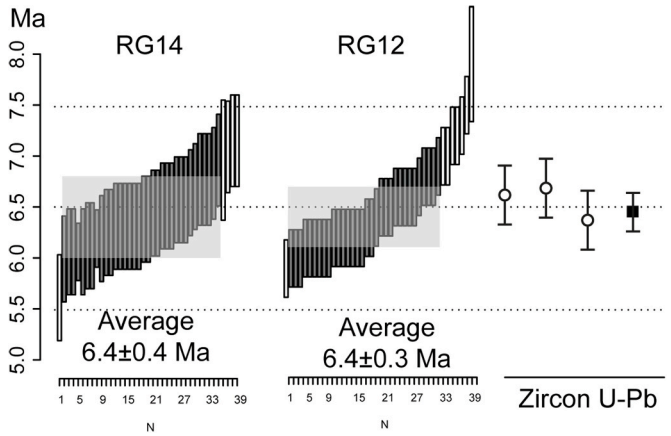

Fig. 17. $^{206}Pb/^{238}U$ zircon data for RG14 and RG12 samples. U–Pb data are ordered and shown as vertical bars comprising 2sigma errors. Grey filled bars were considered for calculation of weighted average ages (horizontal hemi transparent boxes). Available U–Pb zircon data, with relative errors, for the Porto Azzurro pluton are also shown: white circles refer to SIMS U/Pb ages from three zircon grains in Gagnevin et al. (2011); black square is the LA-ICP-MS U/Pb age of a zircon rim from the contact aureole (Musumeci et al., 2011).

Table 1
Physical parameters used in the thermal model.

Parameter	Symbols and equations	Values
Thermal conductivity [W m^{-1} K^{-1}]	K	1.85 (crust) 3.35 (mantle)
Density [kg m^{-3}]	ρ	2750 (crust) 3300 (mantle)
Specific heat [J kg^{-1} K^{-1}]	C_P	1000 (crust) 1100 (mantle)
Heat generation rate [μW m^{-3}]	$A = A_0\, e^{(-z/D)}$	$A_0 = 2$ $D = 12000$ m
Latent heat of crystallization [kJ kg^{-1}]	ΔH	300 (for a T range of 850-650 °C)
Unroofing rate [m yr^{-1}]	$v_z = dz/dt = -c\ z$	$v_{z\ (t=0)} = 5 \times 10^{-3}$ m yr^{-1} $c = 8.93 \times 10^{-7}$ yr^{-1}

pressure value.

For the estimation of the ductile strength we used the power-law dislocation creep equation (see Ranalli, 1995):

$$\frac{d\varepsilon}{dt} = A_c \sigma^n exp\left(-\frac{E}{RT}\right) \quad (5)$$

where $d\varepsilon/dt$ is the strain rate, σ is differential stress, A_c, n and E are creep parameters, R is the gas constant and T is the temperature.

Selected values are as follows: a pore fluid pressure factor (λ) of 0.9, a

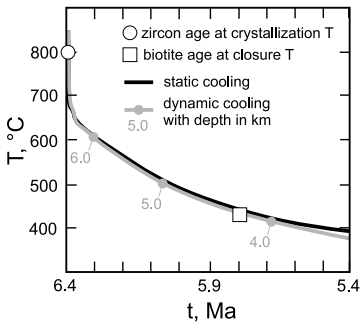

Fig. 18. T-t diagram showing the cooling history of the Porto Azzurro monzogranitic pluton reproduced for 1 Myr after the magma emplacement fixed at 6.4 Ma at a depth of c. 6.5 km. The two cooling curves result from a static model (black line) and a dynamic model (grey line), incorporating the effect of unroofing simulated by an exponential law (see Table 1). Details of the modelling are provided in Caggianelli et al. (2018) and Caggianelli et al. (2014). Age obtained from zircon is plotted at the corresponding saturation temperature. Age of biotite (Maineri et al., 2003) is plotted at the corresponding closure temperature, calculated by Dobson (1973) formula.

β value of 0.75 adequate for an extensional tectonic context, and a strain rate of 1×10^{-14} s^{-1} during ductile deformation by dislocation creep mechanism. The flow law parameters of quartzite and granite (Ranalli, 1995) have been used for roof rocks and Porto Azzurro monzogranite, respectively (Table 2). Depth-strength diagrams at 300, 600 and 1000 kyr are provided in Fig. 19. According to the static model, the B/D (brittle/ductile) transition at 300 kyr is in the roofing rocks at $z = 5$ km, well above the contact with the underlying monzogranite, located at c. 6.4 km. At 600 kyr the B/D transition deepens ($z = 5.6$ km) but still remains above the wall rock - pluton contact. However, the lithological change from wall rock to granite generates a passage to the brittle domain and the appearance of a second B/D transition at a depth of 6.8 km. Consequently, at this time the top of the pluton is already entered into the brittle domain. At 1 Myr, the shallower B/D transition disappears and the deeper one drifts to a depth of 7.8 km well within the plutonic body. The dynamic model (Fig. 19b) differs in producing shallower B/D transitions and in anticipating the passage to the brittle domain owing to the faster cooling of the pluton and roof rocks.

The evolution of the B/D transitions for 1 Ma starting from magma emplacement is portrayed in the diagram of Fig. 20 for both the static and dynamic conditions. In the static case, it can be seen that the minimum depth of the B/D transition (c. 5 km) occurs at c. 250 kyr (point x in Fig. 20a). Instead, the genesis of the second B/D transition takes place at c. 500 kyr (point z). Finally, at 900 kyr the shallower B/D transition (point y) disappears and all the wall rocks pass to the brittle domain. In the dynamic case, the passage of the top of the monzogranite to the brittle domain (point z in Fig. 20b) is anticipated by about 120 kyr (i.e. at c. 380 kyr), whereas the shallower B/D transition culminates after c. 500 kyr at a minimum depth of c. 3.6 km (point x) and disappears after c. 750 kyr (point y). Afterwards, the whole plutonic body, with the exception of the deepest part, migrates into the brittle domain.

5. Final exhumation: (U–Th)/He dating

For the sake of completing the exhumation history of the Porto Azzurro monzogranite (sample RG12), the apatite He ages provide the best constraints on when the exhumation event ceased. In this view we performed (U–Th)/He thermo-chronology on apatite yielding an age of 5.0 ± 0.6 Ma (for more detail see Table A4, in Appendix) related to an assumed T of c. 60 °C.

Therefore, the pluton apatite He age is 1.4 ± 0.6 Myr younger than the zircon U–Pb age, suggesting that within less than 2 million years after emplacement the pluton had exhumed and cooled. It is likely that over this time interval the geothermal gradient (g) was still high, as measured in geothermal areas subjected to shallow magma intrusion and exhumation (e.g. Larderello, Dini et al., 2005; Taupo, Rowland and Sibson, 2004; Los Humeros, Prol-Ledesma and Morán-Zenteno, 2019).

Assuming a thermal gradient of c. 100 °C per km, an averaged exhumation rate in the order of 4.0 mm/yr is possible, higher than the average value of c. 3.4 mm/yr during the first 1 Myr in the modeled cooling history. This suggests an acceleration of the exhumation history in its last part.

6. Discussion

The meso-structural analysis, together with the kinematic study, indicate that the tectonic context in which monzogranite emplacement and deformation took place is extensional. Almost vertical N- and NE-striking faults and felsic dykes (i.e. first generation faults, Fig. 5), as well as low-to middle-angle normal faults (second generation faults, Figs. 3 and 5) and later NW-striking oblique-slip faults (third generation faults, Fig. 5) are framed in the common deformational setting of the CPA (Capoliveri-Porto Azzurro) transfer zone (Fig. 2b), as already described by Liotta et al. (2015). The study area, in fact, is exactly located along the transfer zone. Here, the interplay between the Zuccale extensional detachment and those structures forming the transfer zone (i.e. N-, NE- and NW-striking sub-vertical oblique-to strike-slip faults) caused the localized increase of the permeability, favoring the magma migration through the transfer zone and its emplacement at shallow crustal level (Caggianelli et al., 2018, with references therein). Normal and strike-/oblique-slip faulting assisted the magma intrusion and continued their activity also during magma cooling, promoting injections of felsic dykes along sub-vertical dilatational fractures, affecting the monzogranite and the hosting rocks. This is consistent with failure envelopes (Cox, 2010) favoring fracture permeability development at shallow crustal levels in extensional and strike slip contexts.

The Zuccale detachment played the role of an unroofing fault system during magma cooling (Smith et al., 2011), while the coexisting transfer faults separated crustal volumes with different amounts of extension and of vertical movements (Liotta et al., 2015). It is this mechanism that controlled fast uplift of the extending crust and the progressive exhumation of the magmatic bodies.

Fast exhumation implies two main regional factors: (i) high heat flux, promoting a decrease of rock density and, (ii) relatively high extensional strain rate ($\geq 1x10^{-14}s^{-1}$, Ranalli, 1995). Since the first factor can be easily linked to magma emplacement, extensional strain rate is conversely computed considering restored balanced regional geological sections (Carmignani et al., 1994; Dallmeyer and Liotta, 1998), resulting in 3×10^{-14} s^{-1}, during the Miocene. Locally, in Elba, even greater values can be indicated referring to the Zuccale fault activity, encompassed between 7 and 5 Ma (Westerman et al., 2004; Dini et al., 2008) and resulting in a total throw of 6 km (Pertusati et al., 1993). Considering these data, an average slip rate of about 3 mm/yr at least can be assumed. Collettini et al. (2009) explain these relevant values considering metamorphic reactions caused by fluid-rock interactions and

Table 2
Flow law constants adopted for the dislocation creep exponential equation.

	Lithology	Rheological analog	Creep parameters		
			A_c [$MPa^{-n}s^{-1}$]	n	E [J mol^{-1}]
Roof rock	micaschist and quartzite	wet quartzite	3.2×10^{-4}	2.3	1.54×10^5
Pluton	monzogranite	granite	1.80×10^{-9}	3.2	1.23×10^5

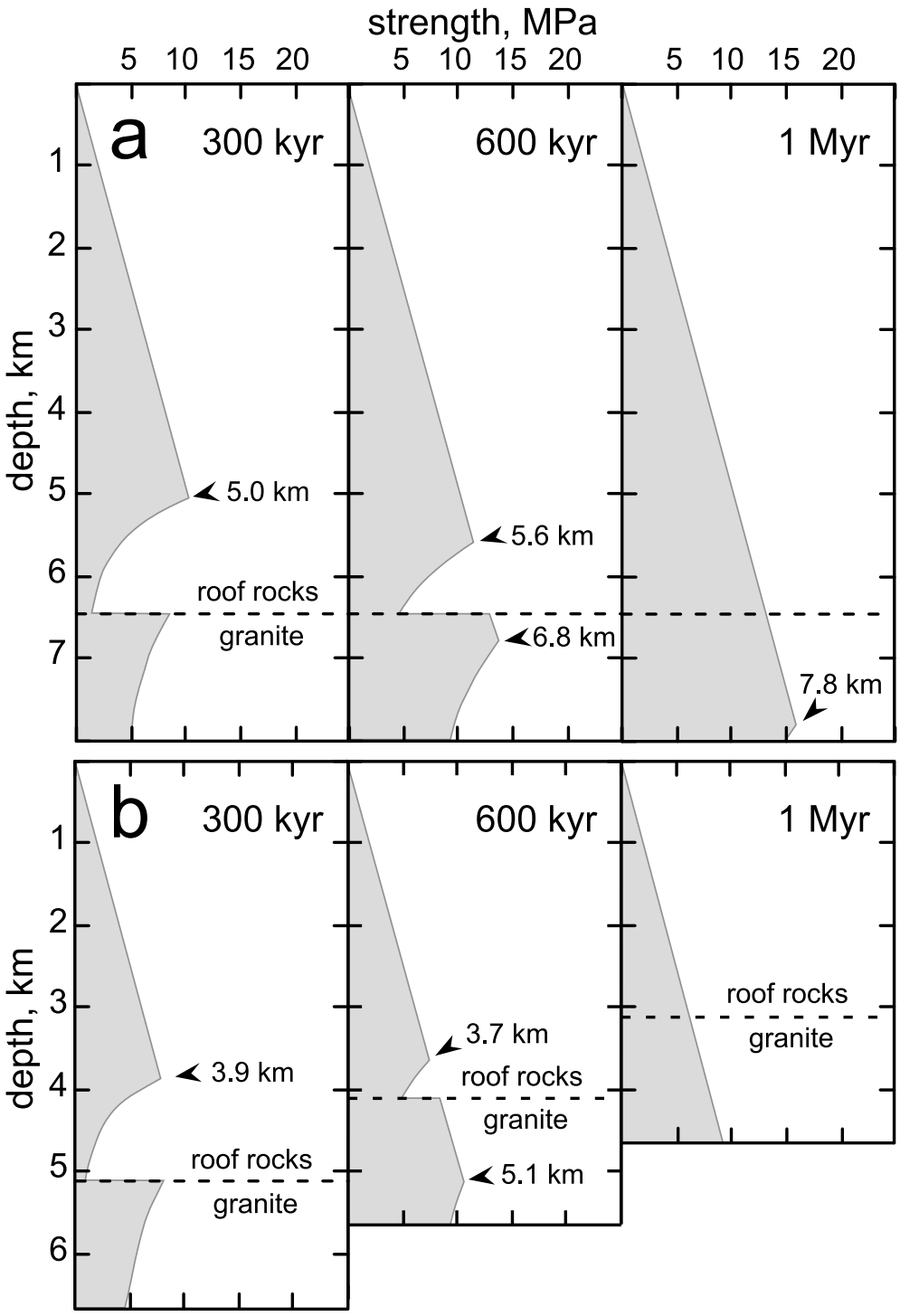

Fig. 19. Depth - strength diagrams at 300 kyr, 600 kyr and 1 Myr. They show depth of the brittle/ductile transitions and the contact between the Porto Azzurro monzogranite with the roof rocks. (a) Static model; (b) dynamic model incorporating the effect of unroofing.

determining talc inducing fault-weakening. In the same line, we have evidence for syn-tectonic injection of lower density melt in the slip zone of the fault at the roof of the monzogranite, thus promoting fault-weakening, too. A further element acting for fault weakening is represented by the occurrence of graphite along the slip surfaces and within the damage zone of normal faults affecting the hosting rocks (Liotta et al., 2015) and responsible for unroofing the Porto Azzurro monzogranite.

In the time interval from 6.4 to 5 Ma, exhumation rate is determined to be between 3.4 and 3.9 mm/yr, as estimated on the basis of geochronological, thermo-chronological data and on the modeling. This rate exceeds the so far determined values for inland Tuscany (Balestrieri et al., 2003, 2011; Fellin et al., 2007; Thomson et al., 2010; Abbate et al., 1994; Carminati et al., 1999; Coli, 1989), where the highest values (1.3–1.8 mm/yr) have been determined, on the basis of fission tracks analysis on apatite and zircon, during late Miocene, after and before periods where exhumation rate is lesser than 1 mm/yr (Balestrieri et al., 2003; Fellin et al., 2007; Thomson et al., 2010).

The difference between the Porto Azzurro exhumation rate and those reported for Tuscany, is explained by the: (i) significant enhancement of

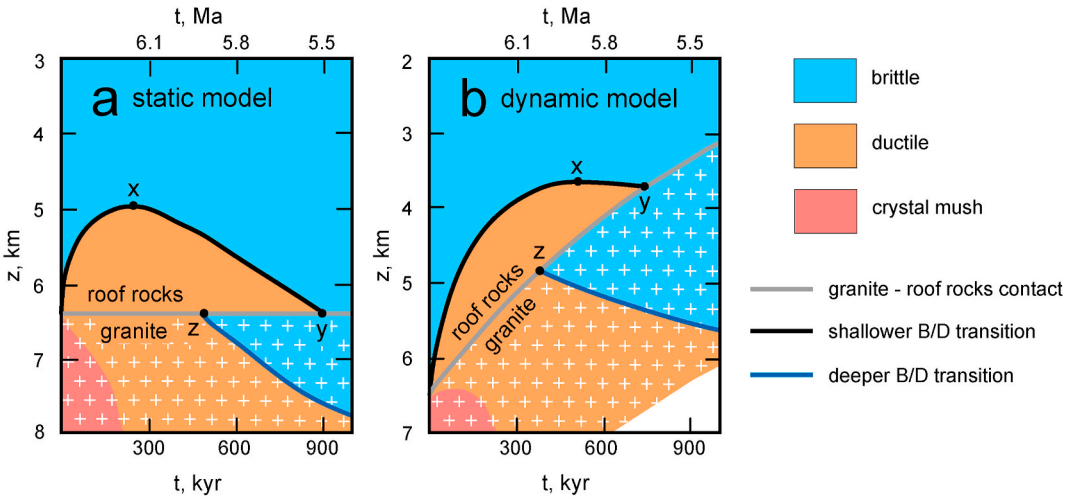

Fig. 20. z-t diagram showing the depth change of the rheological boundaries (black and blue lines) and of the monzogranite - roof rocks lithological boundary (grey line), as reproduced by a static (a) and dynamic model (b). The simulation lasts 1 Myr starting from 6.4 Ma and from a magma emplacement depth of 6.5 km. The shallower brittle-ductile (B/D) transition (black line), within the roof rocks, culminates to a minimum depth in correspondence of point x and disappears after point y. The deeper B/D transition (blue line), within the monzogranite, starts from point z and progressively sinks. The co-existence of B/D transitions is confined to the time interval between z and y points. The rheological evolution of the top of the pluton, relevant for the Capo Bianco outcrop, can be followed along the grey line. Thus, the points z and y mark the transition to the brittle domain for the monzogranite and the roof rocks, respectively. (For interpretation of the references to color in this figure legend, the reader is referred to the Web version of this article.)

lithospheric stretching and high heat flow; (ii) localized magma emplacement; (iii) rapid granite unroofing, as suggested by the slip rate of Zuccale fault, and consequent fast cooling rate. Significantly, this localized high exhumation occurred during an acceleration of the regional exhumation documented for the late Miocene (Balestrieri et al., 2003; Fellin et al., 2007; Thomson et al., 2010).

Reasonably, the above mentioned processes are linked to the migration of the brittle/ductile transition toward shallower crustal levels, as a consequence of the thermal perturbation induced by monzogranite emplacement which promoted the weakening of the upper crust. The melt and hydrothermal fluid migrations caused acceleration of fault slip rates.

Field evidence indicates that the brittle/ductile migration was a quick event, since ductile deformational features are limited to localized melt-assisted shear zones, followed by high temperature fluid flow within discrete zones.

In fact, microstructural analysis of the felsic dyke (Fig. 7c) suggests high deformation temperatures. These allowed boudinaged Kfs to recrystallize ductilely, quartz to deform by prism <a> slip and hence consistent with ductile Kfs-recrystallization. Prism <c> slip at geological strain rates is typical for granulite facies conditions, at temperatures higher than 650 °C (Mainprice et al., 1986), whereas prism <a> slip is consistent with upper amphibolite facies conditions (Schmid and Casey, 1986) and therefore at about 600 °C.

The microstructural interrelationships support that deformation of the felsic dyke occurred after melt-present monzogranite deformation. Strain softening due to fluid flow along the dykes will have allowed faster strain rates than are typically registered during main geological deformation events, and will have been in the order of $1 \times 10^{-9} s^{-1}$ (e.g. Tullis et al., 1973; Kruhl, 1998; Okudaira et al., 1998), a value that is compatible with the slip-rate of the Zuccale fault.

Quartz-rich hydrothermal vein sample RG4 shows deformation microstructures formed during lower temperature conditions than those preserved within sample RG2. In sample RG4 we have studied the transition from foliated monzogranite to the tourmaline-bearing quartz-rich vein which is accompanied by the evolution from a mylonitic to an ultramylonitic fabric. Fig. 7e suggests that mylonitic deformation of the monzogranite next to the vein, as well as of the vein itself, was triggered by fluid-induced weakening. Since the dyke and vein are close to one another (just 10 m), deformation along both discrete shear zones must have occurred at different times after the monzogranite crossed the brittle-ductile transition boundary during cooling and exhumation. By considering the thermo-rheological evolution depicted in Figs. 18 and 20b, it can be deduced that the monzogranite, close to the roof rocks, entered the brittle field at 480 °C after 380 kyr had elapsed after pluton emplacement. This is a minimum estimate for the timing of the dyke injection and dyke deformation, considered that a brittle behavior of the monzogranite is necessary for a dyking process.

Quartz CPOs of the mylonitic monzogranite next to the tourmaline-bearing quartz-rich vein suggest deformation temperatures of about 450 °C (Fig. 15a). This implies that hydrothermal vein deformation has occurred c. 550 kyr after monzogranite emplacement (see Fig. 18). A deformation temperature difference of >150 °C between the dyke and the vein is supported by the quartz pole figures that suggest rhombohedral <a> slip together with basal <a> slip and subordinated prism <a> slip (Passchier and Trouw, 2005) for deformation of the vein.

This reconstruction unveils that the fast transition into the brittle domain, still involves ductile deformation, in contrast with what is expected for quickly cooling upper crustal granitic plutons (Caggianelli et al., 2000; Moyen et al., 2003; de Saint-Blanquat et al., 2006; Gonzáles Guillot et al., 2018; Liu et al., 2020).

7. Conclusions

The integration among meso- and microstructural analyses, geochronological, thermo-chronological studies and modeling allows us to state that Porto Azzurro monzogranite emplaced, on the basis of our new dataset, at 6.4 ± 0.4 Ma in the upper crust (about 6.5 km depth) in an extensional setting, within a transfer zone of crustal relevance. Consequently, it experienced fast cooling and a quick transition into the brittle regime. Nevertheless, this is marked by ductile deformation, within discrete melt- and fluid-assisted shear zones, as highlighted by EBSD data of ductilely deformed K-feldspar and quartz.

The thermo-rheological model indicates that the upper part of the monzogranite entered into the brittle domain c. 380 kyr after its emplacement, allowing dyke formation and melt-injection that triggered localized high strain ductile deformation. The subsequent stage of ductile deformation happened at c. 170 kyr later, and affected quartz-rich veins at lower temperatures, most likely due to enhanced fluid-flow within the localized shear zones.

The cooling history of the pluton developed during fast exhumation, with an estimated rate ranging from c. 3.4–4.0 mm/yr, and was promoted by transfer faults working in concert with dilational and unroofing faults in the frame of the Neogene extensional tectonics.

The key-message of our conclusion is that ductile deformation can affect a granitic intrusion even when it is already entered into the brittle domain, due to localized thermo-rheological perturbations, caused by late magmatic and hydrothermal events, in an extensional regime.

Declaration of competing interest

The authors declare that they have no known competing financial interests or personal relationships that could have appeared to influence the work reported in this paper.

Acknowledgments

We acknowledge Andrea Dini for the discussion on the Elba magmatism and for its guidance in the main outcrops described in this paper. We gratefully thank an anonymous referee for his/her very constructive suggestions and comments that significantly improved the manuscript. We also warmly thank the editor Joao Hippertt for handling our manuscript and his helpful advises. A.B, A.C., C.B., D.L., M.Z. received funding from the European Community's Seventh Framework Programme under grant agreement No. 608553 (Project IMAGE). R.S thanks the grants DOR1827303 of the University of Padova and of Italian PRIN 20178LPCP.

Appendix. Analytical methods

During this investigation we used scanning electron microscopes (SEMs) for: (i) quantitative chemical analysis; (ii) electron backscatter diffraction (EBSD) analysis; (iii) backscattered electron (BSE) imaging, and (iv) CL-imaging. We used an EVO Zeiss SEM at Bari University, a CamScan 2500 SEM equipped with a NordlysNano (Oxford Instruments) EBSD detectors at University of Padova, a Philips XL30 electron microscope equipped with a Centaurus CL detector at Pavia CNR-IGG-UOS, respectively. In situ zircon U–Pb geochronology was determined by LA-ICP-MS at CNR-IGG-UOS of Pavia.

In situ U–Pb geochronology was determined by excimer LA-ICP-MS at CNR-IGG-UOS of Pavia. Zircons were separated by conventional methods (crushing, heavy liquids, hand picking) from two samples (RG12; RG14). Prior to age determination, the internal structure of the zircon grains was investigated with backscattered electron (BSE) and Cathodoluminescence (CL) images using a Philips XL30 electron microscope equipped with a Centaurus CL detector. Images were obtained using 15 kV acceleration and a working distance of 26 mm.

Age determinations were performed using a 193 nm ArF excimer laser microprobe (GeoLas200QMicrolas) coupled to a magnetic sector ICP-MS (Element 1 from ThermoFinnigan). Analyses were carried out in single spot mode and with a spot size fixed at 25 mm. The laser was operated with a frequency of 5 Hz, and with a fluence of 8 J/cm2. Sixty seconds of background signal and at least 30 s of ablation signal were acquired. The signals of masses 202Hg, 204(PbHg), 206 Pb, 207 Pb, 208 Pb, 232Th, and 238U were acquired in magnetic scan mode. 235U is calculated from 238U based on the mean ratio 238U/235U of 137.818, as recently proposed by Hiess et al. (2012). The 202 and 204 masses were collected in order to monitor the presence of common Pb in zircon. Mass bias and laser-induced fractionation were corrected by adopting external standards, the GJ-1 zircon standard (608.56 ± 0.4 Ma; Jackson et al., 2004). During an analytical run of zircon analyses, a reference zircon 91,500 (Widenbeck et al., 1995) was analyzed together with unknowns for quality control. Data reduction was carried out through the GLITTER software package (Van Achterbergh et al., 2001). Time-resolved signals were carefully inspected to detect perturbation of the signal related to inclusions, cracks, or mixed-age domains. Within the same analytical run, the error associated with the reproducibility of the external standards was propagated to each analysis of sample (see Horstwood et al., 2003), and after this procedure each age determination was retained as accurate within the quoted error. The Concordia test was performed for each analytical spot from 206 Pb/238U and 207 Pb/235U ratios using the function in the software package Isoplot/Ex 3.00 [Ludwig, 2003]. Percentage of discordance has been calculated as {[1-(206 Pb/238U age/207 Pb/235U age)] x 100}. Errors in the text and figures are reported as 2sigma. The IsoplotR software (Vermeesch, 2018) was used to draw diagrams of age data. U–Pb isotope analyses and calculated ages of zircons are reported in the data repository (Table A3).

Single crystal apatite (U–Th)/He dating has been undertaken at Scottish Universities Environmental Research Centre. Individual apatite grains were screened based on their clarity and morphology, and hand-picked for (U–Th)/He analysis then packed into Pt tubes prior to analysis. Helium, U and Th analytical protocols adopted in this study follows those described by Foeken et al. (2006, 2007). Length and width measurements for alpha ejection correction (FT; Farley, 2002), were taken for each grain. (U–Th)/He dates were calculated using standard procedures developed by Meesters and Dunai (2002). Total analytical uncertainty, computed as a square root of squares of weighted uncertainties of U, Th and He measurements, and including the estimated additional variation of ±7% determined on repeat analyses of Durango apatite. Data are reported in table A4.

Table A1
Selected analyses of mineral phases in monzogranite (RG 14) and in a felsic dyke (LCA 7).

	RG 14							LCA 7						
	Pl core	Pl core	Pl rim	Kfs	Ab	Bt	Bt	Pl core	Pl rim	Kfs	Bt	Bt	Tur core	Tur rim
SiO_2	59.13	59.18	65.37	65.40	68.41	35.73	36.79	65.18	65.83	64.11	33.57	34.62	35.76	35.49
TiO_2						4.18	3.97				3.66	3.11	0.47	0.86
Al_2O_3	26.48	25.38	21.68	18.48	19.64	16.90	16.20	21.70	21.79	18.40	17.81	18.97	34.45	34.23
FeO						19.73	19.33			0.23	24.83	23.63	9.46	10.05
MnO											0.37	0.38		
MgO						8.47	9.04				4.55	4.73	3.14	3.16
CaO	8.30	7.49	3.06		0.44			2.78	2.79	0.17			0.20	0.48
Na_2O	6.97	7.23	9.75	1.20	10.97	0.33	0.31	9.78	9.58	1.38		0.18	1.54	1.70
K_2O	0.15	0.36	0.27	15.56	0.30	9.63	9.59	0.39	0.24	15.15	9.78	9.80	0.09	
B_2O_3*													10.47	10.51
Li_2O**													0.25	0.27
Tot.	101.03	99.64	101.13	100.64	99.76	94.97	95.23	99.83	100.24	99.44	94.58	95.41	95.83	96.75

(continued on next page)

Table A1 (*continued*)

	RG 14							LCA 7						
	Pl core	Pl core	Pl rim	Kfs	Ab	Bt	Bt	Pl core	Pl rim	Kfs	Bt	Bt	Tur core	Tur rim
∑O	8	8	8	8	8	11	11	8	8	8	11	11	29eLi	29eLi
Si	2.615	2.652	2.873	2.997	2.993	2.744	2.805	2.873	2.883	2.979	2.671	2.700	5.938	5.868
Ti						0.241	0.227				0.219	0.182	0.059	0.107
Al^{IV}	1.282	1.342	1.124	0.999	1.014	1.256	1.195	1.129	1.126	1.009	1.672	1.746	0.062	0.132
Al^{VI}						0.275	0.262						6.687	6.546
Fe						1.267	1.233			0.009	1.652	1.541	1.313	1.389
Mn											0.025	0.025		
Mg						0.97	1.027				0.540	0.550	0.777	0.779
Ca	0.393	0.360	0.144		0.021			0.131	0.131	0.008			0.036	0.085
Na	0.598	0.628	0.831	0.107	0.930	0.049	0.046	0.836	0.814	0.124		0.027	0.496	0.561
K	0.008	0.021	0.015	0.909	0.017	0.943	0.932	0.022	0.013	0.898	0.992	0.975	0.019	
B													3.000	3.000
Li													0.164	0.179
∑cat	4.997	5.002	4.988	5.012	4.974			4.991	4.967	5.028	7.770	7.746	18.550	18.550
X_{Fe}						0.566	0.546				0.754	0.737	0.628	0.641

* B_2O_3 calculated assuming 3 B atoms per formula unit. ** Li_2O calculated by charge balance.

Table A2
Selected analyses of accessory phases in monzogranite (RG14) and felsic dyke (LCA 7).

	RG 14				LCA 7	
	Zrc	Mnz	Mnz	Ap	Zrc	Mnz
SiO_2	31.35	2.25	1.23	0.19	29.65	0.60
FeO	0.34			0.82		
MnO				0.67		
CaO		0.54	0.69	55.11		1.55
Na_2O				0.12		
P_2O_5		26.50	28.05	43.13		29.19
La_2O_3		16.28	15.54			13.85
Ce_2O_3		30.00	31.00			28.42
Pr_2O_3		2.37	3.19			2.80
Nd_2O_3		10.10	11.32			11.63
Sm_2O_3			1.38			2.37
Gd_2O_3						1.74
ThO_2	0.97	11.42	8.11			7.14
UO_2	1.26				5.68	0.74
Sc_2O_3					0.54	
ZrO_2	65.04				61.00	
HfO_2	0.34				1.50	
Tot.	99.30	99.46	100.51	101.04	98.38	100.02
∑O	4	4	4	25	4	4
Si	0.982	0.091	0.049	0.031	0.955	0.024
Fe	0.009			0.113		
Mn				0.093		
Ca		0.023	0.029	9.706		0.065
Na				0.038		
P		0.911	0.946	6.002		0.974
La		0.244	0.228			0.201
Ce		0.446	0.452			0.410
Pr		0.035	0.046			0.040
Nd		0.146	0.161			0.164
Sm			0.019			0.032
Gd						0.023
Th	0.007	0.105	0.074			0.064
U	0.008				0.041	0.006
Sc					0.015	
Zr	0.984				0.958	
Hf					0.014	
∑cat	2.000	2.002	2.005	15.984	1.983	2.004

Appendix A. Supplementary data

Supplementary data to this article can be found online at https://doi.org/10.1016/j.jsg.2021.104326.

Table A3
LA-ICP-MS isotopic data of zircon from RG12 and RG14 samples.

Data for Wetherill plot[3]									Ages[3]								
Spot Position	Zoning	$^{207}Pb/2^{06}$ Pb	1σ %	^{207} Pb/^{235}U	1σ %	^{206}Pb/^{238}U	1σ %	Rho	^{207}Pb/^{206}Pb	1σ abs	^{207}Pb/^{235}U	1σ abs	^{206}Pb/^{238}U	1σ abs	% U–Pb disc[4]	Concordant age	2σ abs
rim	oscill	0.04950	0.00148	**0.00761**	**0.00021**	**0.00112**	**0.00002**	**0.7**	171.6	5.1	7.7	0.2	7.2	0.1	6.3		
rim	oscill	0.05477	0.00202	**0.00848**	**0.00030**	**0.00112**	**0.00002**	**0.6**	402.8	14.9	8.6	0.3	7.2	0.1	15.8		
core	oscill	0.04710	0.00141	**0.00737**	**0.00020**	**0.00114**	**0.00002**	**0.7**	54.3	1.6	7.5	0.2	7.3	0.1	1.5	7.3	0.30
rim	oscill	0.05143	0.00177	**0.00675**	**0.00022**	**0.00095**	**0.00002**	**0.7**	260.1	8.9	6.8	0.2	6.1	0.1	10.4		
rim	oscill	0.04670	0.00398	**0.00750**	**0.00063**	**0.00117**	**0.00002**	**0.2**	33.9	2.9	7.6	0.6	7.5	0.1	0.6	7.5	0.30
rim/core	oscill	0.07078	0.00256	**0.01035**	**0.00035**	**0.00106**	**0.00002**	**0.6**	951.1	34.4	10.5	0.4	6.8	0.1	34.7		
rim	homog	0.07040	0.00209	**0.00939**	**0.00026**	**0.00097**	**0.00002**	**0.8**	940.0	27.9	9.5	0.3	6.2	0.1	34.1		
rim	oscill	0.05475	0.00170	**0.00716**	**0.00021**	**0.00095**	**0.00002**	**0.8**	402.0	12.5	7.2	0.2	6.1	0.1	15.5		
core	homog	0.04778	0.00239	**0.00636**	**0.00031**	**0.00097**	**0.00002**	**0.5**	88.4	4.4	6.4	0.3	6.2	0.1	2.9		
rim/core	oscill	0.05439	0.00224	**0.00730**	**0.00029**	**0.00097**	**0.00002**	**0.6**	387.2	16.0	7.4	0.3	6.2	0.1	15.4		
rim	oscill	0.04944	0.00150	**0.00691**	**0.00020**	**0.00102**	**0.00002**	**0.8**	168.8	5.1	7.0	0.2	6.6	0.1	6.0		
core	oscill	0.04630	0.00578	**0.00592**	**0.00073**	**0.00093**	**0.00002**	**0.2**	13.3	1.7	6.0	0.7	6.0	0.1	0.0	6.0	0.30
rim	oscill	0.05693	0.00167	**0.00831**	**0.00022**	**0.00106**	**0.00002**	**0.8**	488.8	14.4	8.4	0.2	6.8	0.1	18.7		
rim	oscill	0.04888	0.00202	**0.00672**	**0.00026**	**0.00100**	**0.00002**	**0.6**	142.1	5.9	6.8	0.3	6.4	0.1	5.3		
rim	oscill	0.04981	0.00206	**0.00643**	**0.00025**	**0.00094**	**0.00002**	**0.6**	186.1	7.7	6.5	0.3	6.1	0.1	6.9		
rim	oscill	0.06913	0.00240	**0.00871**	**0.00028**	**0.00092**	**0.00002**	**0.7**	902.6	31.3	8.8	0.3	5.9	0.1	32.7		
rim	oscill	0.04913	0.00448	**0.00827**	**0.00075**	**0.00122**	**0.00002**	**0.2**	154.0	14.1	8.4	0.8	7.9	0.2	6.0		
rim	oscill	0.05566	0.00225	**0.00736**	**0.00028**	**0.00096**	**0.00002**	**0.6**	438.8	17.7	7.4	0.3	6.2	0.1	16.9		
rim	oscill	0.05372	0.00161	**0.00757**	**0.00021**	**0.00102**	**0.00002**	**0.8**	359.3	10.8	7.7	0.2	6.6	0.1	14.2		
rim	oscill	0.05118	0.00181	**0.00716**	**0.00025**	**0.00101**	**0.00002**	**0.6**	248.9	8.8	7.2	0.2	6.5	0.1	10.2		
rim	oscill	0.04859	0.00152	**0.00705**	**0.00021**	**0.00105**	**0.00002**	**0.7**	128.1	4.0	7.1	0.2	6.8	0.1	5.2		
rim	oscill	0.05028	0.00170	**0.00711**	**0.00023**	**0.00103**	**0.00002**	**0.7**	208.0	7.0	7.2	0.2	6.6	0.1	7.7		
rim	oscill	0.06063	0.00213	**0.00816**	**0.00027**	**0.00098**	**0.00002**	**0.7**	626.1	22.0	8.3	0.3	6.3	0.1	23.5		
rim	oscill	0.07312	0.00210	**0.00951**	**0.00026**	**0.00094**	**0.00002**	**0.9**	1017.3	29.2	9.6	0.3	6.1	0.1	37.0		
rim/core	oscill	0.05588	0.00256	**0.00837**	**0.00037**	**0.00109**	**0.00002**	**0.5**	447.6	20.5	8.5	0.4	7.0	0.1	17.0		
rim	oscill	0.05122	0.00160	**0.00756**	**0.00022**	**0.00107**	**0.00002**	**0.7**	250.7	7.8	7.6	0.2	6.9	0.1	9.9		
rim	oscill	0.05050	0.00183	**0.00699**	**0.00024**	**0.00101**	**0.00002**	**0.6**	218.1	7.9	7.1	0.2	6.5	0.1	8.0		
rim	oscill	0.04789	0.00185	**0.00666**	**0.00024**	**0.00101**	**0.00002**	**0.6**	93.8	3.6	6.7	0.2	6.5	0.1	3.4		
rim	oscill.	0.05215	0.00357	**0.00732**	**0.00050**	**0.00102**	**0.00002**	**0.3**	292	20.0	7.4	0.5	6.6	0.1	11.3		
rim	oscill.	0.05168	0.00254	**0.00683**	**0.00034**	**0.00096**	**0.00001**	**0.2**	271	13.3	6.9	0.3	6.2	0.1	10.5		
rim	oscill.	0.06402	0.00329	**0.00854**	**0.00044**	**0.00097**	**0.00002**	**0.4**	742	38.2	8.6	0.4	6.2	0.1	27.6		
rim	oscill.	0.05069	0.00212	**0.00711**	**0.00030**	**0.00102**	**0.00002**	**0.5**	227	9.5	7.2	0.3	6.6	0.1	8.6		
rim	oscill.	0.04691	0.00202	**0.00620**	**0.00027**	**0.00096**	**0.00001**	**0.3**	45	1.9	6.3	0.3	6.2	0.1	1.4	6.2	0.14
rim	oscill.	0.06156	0.00275	**0.00879**	**0.00039**	**0.00104**	**0.00002**	**0.4**	659	29.5	8.9	0.4	6.7	0.1	24.6		
rim	oscill.	0.04615	0.00706	**0.00693**	**0.00105**	**0.00109**	**0.00002**	**0.1**	5	0.8	7.0	1.1	7.0	0.1	−0.1		
rim	oscill.	0.07062	0.00306	**0.00952**	**0.00041**	**0.00098**	**0.00002**	**0.5**	946	41.0	9.6	0.4	6.3	0.1	34.4		
rim	oscill.	0.06392	0.00254	**0.00821**	**0.00032**	**0.00093**	**0.00002**	**0.6**	739	29.4	8.3	0.3	6.0	0.1	27.8		
rim	oscill.	0.05203	0.00204	**0.00670**	**0.00026**	**0.00093**	**0.00001**	**0.3**	287	11.2	6.8	0.3	6.0	0.1	11.6		
rim	oscill.	0.05625	0.00221	**0.00736**	**0.00029**	**0.00095**	**0.00002**	**0.5**	462	18.1	7.4	0.3	6.1	0.1	17.8		
rim	oscill.	0.05349	0.00409	**0.00702**	**0.00054**	**0.00095**	**0.00002**	**0.3**	350	26.7	7.1	0.5	6.1	0.1	13.8		
rim	oscill	0.05561	0.00304	**0.00844**	**0.00047**	**0.00110**	**0.00002**	**0.4**	437	23.9	8.5	0.5	7.1	0.2	17.0		

(*continued on next page*)

Table A3 (*continued*)

Data for Wetherill plot[3]									Ages[3]								
Spot Position	Zoning	$^{207}Pb/2^{06}$ Pb	1σ %	^{207} Pb/^{235}U	1σ %	$^{206}Pb/^{238}U$	1σ %	Rho	$^{207}Pb/^{206}Pb$	1σ abs	$^{207}Pb/^{235}U$	1σ abs	$^{206}Pb/^{238}U$	1σ abs	% U–Pb disc[4]	Concordant age	2σ abs
rim	oscill	0.05015	0.00180	**0.00722**	**0.00027**	**0.00104**	**0.00002**	**0.6**	202	7.2	7.3	0.3	6.7	0.2	8.3		
rim	oscill	0.05264	0.00201	**0.00762**	**0.00029**	**0.00105**	**0.00002**	**0.6**	313	12.0	7.7	0.3	6.8	0.2	12.2		
rim	oscill	0.04696	0.00239	**0.00656**	**0.00034**	**0.00101**	**0.00002**	**0.5**	47	2.4	6.6	0.3	6.5	0.2	2.0	6.51	0.31
rim	oscill	0.05841	0.00213	**0.00790**	**0.00029**	**0.00098**	**0.00002**	**0.7**	545	19.9	8.0	0.3	6.3	0.2	21.0		
rim	broad band	0.06220	0.00989	**0.00840**	**0.00132**	**0.00098**	**0.00002**	**0.2**	681	108.3	8.5	1.3	6.3	0.2	25.7		
rim	oscill	0.05400	0.00312	**0.00726**	**0.00042**	**0.00098**	**0.00002**	**0.4**	371	21.4	7.3	0.4	6.3	0.2	14.0		
rim	oscill	0.04719	0.00252	**0.00666**	**0.00036**	**0.00102**	**0.00002**	**0.4**	59	3.1	6.7	0.4	6.6	0.2	2.5		
rim	oscill	0.05225	0.00250	**0.00707**	**0.00034**	**0.00098**	**0.00002**	**0.5**	296	14.2	7.2	0.3	6.3	0.2	11.7		
rim	oscill	0.05806	0.00213	**0.00823**	**0.00030**	**0.00103**	**0.00002**	**0.6**	532	19.5	8.3	0.3	6.6	0.2	20.3		
rim	oscill	0.07443	0.00553	**0.01110**	**0.00082**	**0.00108**	**0.00002**	**0.3**	1053	78.2	11.2	0.8	7.0	0.2	37.9		
rim	oscill	0.05884	0.00350	**0.00765**	**0.00046**	**0.00094**	**0.00002**	**0.4**	561	33.4	7.7	0.5	6.1	0.2	21.7		
rim	oscill	0.08283	0.00638	**0.01166**	**0.00089**	**0.00102**	**0.00002**	**0.3**	1265	97.5	11.8	0.9	6.6	0.2	44.2		
rim	oscill	0.05245	0.00275	**0.00688**	**0.00037**	**0.00095**	**0.00002**	**0.5**	305	16.0	7.0	0.4	6.1	0.2	12.1		
rim	oscill	0.04710	0.00473	**0.00610**	**0.00061**	**0.00094**	**0.00002**	**0.2**	54	5.5	6.2	0.6	6.1	0.2	1.9	6.06	0.30
rim	oscill	0.06024	0.00391	**0.00776**	**0.00050**	**0.00093**	**0.00002**	**0.4**	612	39.7	7.8	0.5	6.0	0.1	23.7		
rim	oscill	0.05021	0.00232	**0.00659**	**0.00031**	**0.00095**	**0.00002**	**0.5**	205	9.4	6.7	0.3	6.1	0.2	8.2		
rim	oscill	0.04643	0.00295	**0.00651**	**0.00042**	**0.00102**	**0.00002**	**0.4**	20	1.3	6.6	0.4	6.6	0.2	0.3	6.57	0.30
rim	oscill	0.05516	0.00529	**0.00741**	**0.00070**	**0.00098**	**0.00002**	**0.3**	419	40.2	7.5	0.7	6.3	0.2	15.8		
rim	oscill	0.05656	0.00192	**0.00745**	**0.00026**	**0.00096**	**0.00002**	**0.5**	474	16.1	7.5	0.3	6.2	0.1	17.9		
rim	oscill	0.06423	0.00301	**0.00878**	**0.00041**	**0.00099**	**0.00002**	**0.5**	749	35.1	8.9	0.4	6.4	0.2	28.1		
rim	oscill	0.06459	0.00329	**0.00901**	**0.00046**	**0.00101**	**0.00002**	**0.5**	761	38.7	9.1	0.5	6.5	0.2	28.5		
rim	oscill	0.05740	0.00687	**0.00766**	**0.00091**	**0.00097**	**0.00002**	**0.2**	507	60.7	7.7	0.9	6.2	0.2	19.3		
rim	oscill	0.04702	0.00302	**0.00720**	**0.00047**	**0.00111**	**0.00002**	**0.3**	50	3.2	7.3	0.5	7.2	0.2	1.8	7.15	0.32
rim	oscill	0.09611	0.00435	**0.01372**	**0.00062**	**0.00104**	**0.00002**	**0.5**	1550	70.1	13.8	0.6	6.7	0.2	51.6		
rim	broad band	0.05629	0.00274	**0.00815**	**0.00040**	**0.00105**	**0.00002**	**0.5**	464	22.6	8.2	0.4	6.8	0.2	17.9		
rim	oscill	0.04775	0.00232	**0.00690**	**0.00034**	**0.00105**	**0.00002**	**0.5**	87	4.2	7.0	0.3	6.8	0.2	3.1		
rim	oscill	0.09471	0.00239	**0.01381**	**0.00037**	**0.00106**	**0.00002**	**0.8**	1522	38.4	13.9	0.4	6.8	0.2	51.0		
rim	oscill	0.05156	0.00211	**0.00690**	**0.00029**	**0.00097**	**0.00002**	**0.6**	266	10.9	7.0	0.3	6.2	0.2	10.5		
core	oscill	0.05768	0.00157	**0.00751**	**0.00022**	**0.00094**	**0.00002**	**0.6**	518	14.1	7.6	0.2	6.1	0.1	20.3		
rim	oscill	0.04891	0.00313	**0.00659**	**0.00043**	**0.00098**	**0.00002**	**0.4**	144	9.2	6.7	0.4	6.3	0.2	5.3		
rim	oscill	0.04690	0.00212	**0.00646**	**0.00030**	**0.00100**	**0.00002**	**0.5**	44	2.0	6.5	0.3	6.4	0.2	1.5	6.44	0.31
rim	oscill	0.04675	0.00323	**0.00620**	**0.00043**	**0.00096**	**0.00002**	**0.4**	36	2.5	6.3	0.4	6.2	0.2	1.4	6.19	0.30
rim	oscill	0.04956	0.00379	**0.00644**	**0.00049**	**0.00094**	**0.00002**	**0.3**	174	13.3	6.5	0.5	6.1	0.2	7.1		
rim	oscill	0.06292	0.00311	**0.00755**	**0.00037**	**0.00087**	**0.00002**	**0.5**	706	34.8	7.6	0.4	5.6	0.1	26.6		
rim	oscill	0.05161	0.00235	**0.00720**	**0.00033**	**0.00101**	**0.00002**	**0.5**	268	12.2	7.3	0.3	6.5	0.2	10.7		
core	oscill	0.05264	0.00338	**0.00728**	**0.00047**	**0.00100**	**0.00002**	**0.4**	313	20.1	7.4	0.5	6.4	0.2	12.5		
rim	oscill	0.04619	0.00210	**0.00705**	**0.00032**	**0.00111**	**0.00002**	**0.5**	8	0.3	7.1	0.3	7.2	0.2	−0.3	7.15	0.32
rim	oscill	0.05184	0.00306	**0.00704**	**0.00042**	**0.00099**	**0.00002**	**0.4**	278	16.4	7.1	0.4	6.4	0.2	10.5		

Table A4
(U + Th)/He data of apatite from RG12 and RG14 samples.

	Capsule name	4He sample (torr)	re-extract (torr)	Total 4He (cc)	Corrected	1 sigma	232Th (ng)	1 sigma error	238U (ng)	1 sigma error	232Th Blk correction	1 sigma error	238U Blk correction	1 sigma error	232Th (ppm)	238U (ppm)	eU (ppm)	Total analytical error (%)
pan4	RG12a-01	2.0E-10	6.9E-11	4.4E-11	3.3E-11	6.1E-12	0.27	0.003	0.05	0.001	0.26	0.004	0.0515	0.0009	214.774	42.332	92.804	1.19%
pan4	RG12a-04	2.4E-10	7.0E-11	5.7E-11	4.4E-11	6.1E-12	0.05	0.001	0.04	0.001	0.03	0.002	0.0397	0.0015	27.566	31.867	38.345	3.53%
pan5	RG12a-07	2.2E-10	6.6E-11	5.6E-11	4.3E-11	3.3E-12	0.06	0.001	0.05	0.001	0.05	0.006	0.0484	0.0008	62.567	58.259	72.962	6.46%
pan5	RG12a-08	1.2E-10	4.0E-11	2.0E-11	1.5E-11	3.2E-12	0.06	0.001	0.04	0.001	0.05	0.006	0.0396	0.0007	74.429	63.496	80.987	7.52%
pan4	RG14a-01	4.4E-10	6.8E-11	1.3E-10	1.1E-10	6.3E-12	0.38	0.004	0.14	0.002	0.37	0.005	0.1349	0.0017	215.778	79.401	130.109	0.97%
pan4	RG14a-03	1.6E-10	6.8E-11	2.9E-11	2.0E-11	6.0E-12	0.07	0.001	0.05	0.001	0.06	0.002	0.0433	0.0010	70.154	48.055	64.542	2.29%
pan4	RG14a-05	2.4E-10	6.1E-11	5.5E-11	4.4E-11	6.1E-12	0.17	0.002	0.08	0.001	0.16	0.003	0.0728	0.0011	110.015	50.071	75.925	1.29%
pan5	RG14a-06	1.9E-10	6.8E-11	4.7E-11	3.4E-11	3.2E-12	0.05	0.000	0.08	0.002	0.03	0.006	0.0816	0.0016	25.213	60.131	66.056	5.72%
pan5	RG14a-07	4.9E-10	6.8E-11	1.6E-10	1.4E-10	4.1E-12	0.16	0.002	0.11	0.001	0.15	0.007	0.1068	0.0012	110.644	78.040	104.041	2.61%
pan5	RG14a-08	2.5E-10	6.8E-11	6.9E-11	5.4E-11	3.4E-12	0.07	0.001	0.12	0.002	0.06	0.006	0.1188	0.0019	36.723	78.141	86.771	3.84%

References

Abbate, E., Balestrieri, M.L., Bigazzi, G., Norelli, P., Quercioli, C., 1994. Fission-track datings and recent rapid denudation in northern Apennines, Italy. Mem. Soc. Geol. Ital. 48, 579–585.

Acocella, V., Funiciello, R., 2006. Transverse systems along the extensional Tyrrhenian margin of central Italy and their influence on volcanism. Tectonics 25. https://doi.org/10.1029/2005TC001845.

Balestrieri, M.L., Bernet, M., Brandon, M.T., Picotti, V., Reiners, P., Zattin, M., 2003. Pliocene and Pleistocene exhumation and uplift of two key areas of the northern Apennines. Quat. Int. 101, 67–73. https://doi.org/10.1016/S1040-6182(02)00089-7.

Balestrieri, M.L., Pandeli, E., Bigazzi, G., Carosi, R., Montomoli, C., 2011. Age and temperature constraints on metamorphism and exhumation of the syn-orogenic metamorphic complexes of Northern Apennines, Italy. Tectonophysics 509, 254–271.

Barberi, F., Brandi, G.P., Giglia, G., Innocenti, F., Marinelli, G., Raggi, R., Ricci, C.A., Squarci, P., Taffi, L., Trevisan, L., 1967. Carta Geologica dell'Isola D'Elba Alla Scala 1:25.000. E.I.R.A., Firenze.

Barchi, M.R., 2010. The Neogene-Quaternary evolution of the Northern Apennines: crustal structure, style of deformation and seismicity. In: Beltrando, M., Peccerillo, A., Mattei, M., Conticelli, S., Doglioni, C. (Eds.), The Neogene-Quaternary Evolution of the Northern Apennines: Crustal Structure, Style of Deformation, Seismicity, Journal of the Virtual Explorer, vol. 36, p. 10pp. https://doi.org/10.3809/jvirtex.2009.00220.

Bartole, R., 1995. The North Tyrrhenian-Northern Apennines post-collisional system: constraints for a geodynamic model. Terra. Nova 7, 7–30.

Bianco, C., Brogi, A., Caggianelli, A., Giorgetti, G., Liotta, D., Meccheri, M., 2015. HP-LT metamorphism in Elba Island: implications for the geodynamic evolution of the inner northern Apennines (Italy). J. Geodyn. 91, 13–25.

Bianco, C., Godard, G., Halton, A., Brogi, A., Liotta, D., Caggianelli, A., 2019. The lawsonite-glaucophane blueschists of Elba Island (Italy). Lithos 348–349, 105198. https://doi.org/10.1016/j.lithos.2019.105198.

Brogi, A., 2006. Neogene extension in the Northern Apennines (Italy): insights from the southern part of the Mt. Amiata geothermal area. Geodin. Acta 19, 33–50.

Brogi, A., 2008. Kinematics and geometry of Miocene low-angle detachments and exhumation of the metamorphic units in the hinterland of the Northern Apennines (Italy). J. Struct. Geol. 30, 2–20.

Brogi, A., 2011. Bowl-shaped basin related to low-angle detachment during continental extension: the case of the controversial Neogene Siena Basin (central Italy, Northern Apennines). Tectonophysics 499, 54–76.

Brogi, A., Liotta, D., 2008. Highly extended terrains, lateral segmentation of the substratum, and basin development: the Middle-Late Miocene Radicondoli Basin (inner northern Apennines, Italy). Tectonics 27. https://doi.org/10.1029/2007TC002188 TC 5002.

Caggianelli, A., Prosser, G., Rottura, A., 2000. Thermal history vs. fabric anisotropy in granitoids emplaced at different crustal levels: an example from Calabria, southern Italy. Terra. Nova 12 (3), 109–116. https://doi.org/10.1046/j.1365-3121.2000.123280.x.

Caggianelli, A., Ranalli, G., Lavecchia, A., Liotta, D., Dini, A., 2014. Post-emplacement thermo-rheological history of a granite intrusion and surrounding rocks: the Monte Capanne pluton, Elba Island, Italy. In: Llan-Fúnez, S., Marcos, A., Bastida, F. (Eds.), Deformation Structures and Processes within the Continental Crust, vol. 394. Geological Society, London, Special Publication, pp. 129–143.

Caggianelli, A., Zucchi, M., Bianco, C., Brogi, A., Liotta, L., 2018. Estimating P-T metamorphic conditions on the roof of a hidden granitic pluton: an example from the Mt. Calamita promontory (Elba Island, Italy). Italian Journal of Geosciences 137, 238–253.

Calcagnile, G., Panza, G.F., 1981. The main characteristics of the Lithosphere Asthenosphere System in Italy and surrounding regions. Pure Appl. Geophys. 119, 865–879.

Carmignani, L., Decandia, F.A., Disperati, L., Fantozzi, P.L., Kligfield, R., Lazzarotto, A., Liotta, D., Meccheri, M., 2001. Inner northern Apennines. In: Vai, G.B., Martini, I.P. (Eds.), Anatomy of an Orogen: the Apennines and Adjacent Mediterranean Basins, 197-213. Springer, Dordrecht. https://doi.org/10.1007/978-94-015-9829-3_14.

Carmignani, L., Decandia, F.A., Disperati, L., Fantozzi, P.L., Lazzarotto, A., Liotta, D., Meccheri, M., 1994. Tertiary extensional tectonics in Tuscany (northern Apennines, Italy). Tectonophysics 238, 295–315.

Carmignani, L., Decandia, F.A., Disperati, L., Fantozzi, P.L., Lazzarotto, A., Liotta, D., Oggiano, G., 1995. Relationships between the Tertiary structural evolution of the Sardinia-Corsica-provençal domain and the northern Apennines. Terra. Nova 7, 128–137.

Carminati, E., Giunghi, C., Argnani, A., Sabadini, R., Fernandez, M., 1999. Plio-Quaternary vertical motion of the Northern Apennines: insights from dynamic modeling. Tectonics 18 (4), 703–718.

Coli, M., 1989. Time and mode of uplift of the Apuane Alps metamorphic complex. Atti Ticinesi Scienze della Terra 32, 47–56.

Collettini, C., Holdsworth, R.E., 2004. Fault zone weakening processes along low-angle normal faults: insights from the Zuccale Fault, Isle of Elba, Italy. J. Geol. Soc. 161, 1039–1052.

Collettini, C., Niemeijer, A., Viti, C., Marone, C., 2009. Fault zone fabric and fault weakness. Nature 462/17, 907–911.

Cox, S.F., 2010. The application of failure mode diagrams for exploring the roles of fluid pressure and stress states n controlling styles of fracture-controlled permeability enhancement in faults and shear zones. Geofluids 10, 217–233. https://doi.org/10.1111/j.1468-8123.2010.00281.x.

Dallmeyer, R.D., Liotta, D., 1998. Extension, uplift of rocks cooling ages in thinned continental provinces: the Larderello geothermal area (inner Northern Apennines, Italy). Geol. Mag. 135, 193–202.

de Saint-Blanquat, M., Habert, G., Horsman, E., Morgan, S.S., Tikoff, B., Launeau, P., Gleizes, G., 2006. Mechanism and duration of non-tectonically assisted magma emplacement in the upper crust: the Black Mesa pluton, Henry Mountains, Utah. Tectonophysics 428, 1–31.

Di Stefano, R., Bianchi, I., Ciaccio, M.G., Carrara, G., Kissling, E., 2011. Three-dimensional Moho topography in Italy: new constraints from receiver functions and controlled source seismology. G-cubed 12 (9), 1–15.

Dini, A., 2003. Ore deposits, industrial minerals and geothermal resources. Per. Mineral. 72, 41–52.

Dini, A., Gianelli, G., Puxeddu, M., Ruggieri, G., 2005. Origin and evolution of pliocene-pleistocene granites from the Larderello geothermal field (Tuscan magmatic province, Italy). Lithos 81, 1–31.

Dini, A., Innocenti, F., Rocchi, S., Tonarini, S., Westerman, D.S., 2002. The magmatic evolution of the Late Miocene laccolith-pluton-dyke granitic complex of Elba Island Italy. Geol. Mag. 139, 257–279.

Dini, A., Westerman, D.S., Innocenti, F., Rocchi, S., 2008. Magma Emplacement in a Transfer Zone: the Miocene Mafic Orano Dyke Swarm of Elba Island, Tuscany, Italy, vol. 302. Geological Society of London Special Publications, pp. 131–148.

Dodson, M.H., 1973. Closure temperature in geochronological and petrological systems. Contrib. Mineral. Petrol. 40, 259–274.

Duranti, S., Palmeri, R., Pertusati, P.C., Ricci, C.A., 1992. Geological evolution and metamorphic petrology of the basal sequences of Eastern Elba (Complex II). Acta Vulca. Mar. 2, 213–229.

Farina, F., Dini, A., Innocenti, F., Rocchi, S., Westerman, D.S., 2010. Rapid incremental assembly of the Monte Capanne pluton (Elba Island, Tuscany) by downward stacking of magma sheets. Geol. Soc. Am. Bull. 122, 1463–1479.

Farley, K.A., 2002. U-Th)/He dating: techniques, calibrations, and applications. Rev. Mineral. Geochem. 47, 819–844. https://doi.org/10.2138/rmg.2002.47.18.

Fellin, M.G., Reiners, P.W., Brandon, M.T., Wüthrich, E., Balestrieri, M.L., Molli, G., 2007. Thermochronologic evidence for the exhumational history of the Alpi Apuane metamorphic core complex, northern Apennines, Italy. Tectonics 26, 1–22. https://doi.org/10.1029/2006TC002085. TC6015.

Foeken, J.P.T., Persano, C., Stuart, F.M., ter Voorde, M., 2007. Role of topography in isotherm perturbation: apatite (U-Th)/He and fission track results from the Malta tunnel, Tauern Window, Austria. Tectonics 26, TC3006. https://doi.org/10.1029/2006TC002049.

Foeken, J.P.T., Stuart, F.M., Dobson, K.J., Persano, C., Vilbert, D., 2006. A diode laser system for heating minerals for (U-Th)/He chronometry. G-cubed 7 Q04015, 1–9. https://doi.org/10.1029/2005GC001190.

Gagnevin, D., Daly, J.S., Horstwood, M.S.A., Whitehouse, M.J., 2011. In-situ zircon U-Pb, oxygen and hafnium isotopic evidence for magma mixing and mantle metasomatism in the Tuscan Magmatic Province, Italy. Earth Planet Sci. Lett. 305, 45–56.

Reheat to heat ratio	Age (Ma)	Real age	Error	Th/U	Error	length	width1	width2	width3	average width	Radius	Termination	F(T) large (U–Th weighted)	Corrected Age	error	238U/ atoms	235U/ atoms	232Th/ atoms	4He/ atoms
34.21%	3.2	2.40	0.04	5.1	0.11	160	60	50		55.0	27.5	1	0.57	4.2	0.4	1.30E+11	9.57E+08	6.78E+11	1.19E+09
29.09%	9.9	7.63	0.35	0.9	0.06	150	60	55		57.5	28.8	1	0.59	13.0	0.7	1.01E+11	7.38E+08	8.92E+10	1.54E+09
30.07%	7.6	5.81	0.49	1.1	0.13	120	55	50		52.5	26.3	0	0.54	10.8	0.9	1.23E+11	9.00E+08	1.35E+11	1.50E+09
33.13%	3.3	2.47	0.25	1.2	0.16	110	50	45		47.5	23.8	1	0.53	4.7	0.5	1.00E+11	7.36E+08	1.21E+11	5.43E+08
15.58%	4.1	3.54	0.05	2.7	0.05	160	70	65	60	65.0	32.5	2	0.63	5.6	0.3	3.41E+11	2.51E+09	9.52E+11	3.41E+09
42.77%	4.0	2.84	0.09	1.5	0.06	130	55	50		52.5	26.3	1	0.64	4.4	0.2	1.09E+11	8.04E+08	1.64E+11	7.70E+08
25.56%	4.1	3.24	0.05	2.2	0.05	170	65	60	50	58.3	29.2	2	0.60	5.4	0.3	1.84E+11	1.35E+09	4.15E+11	1.47E+09
35.44%	4.3	3.15	0.24	0.4	0.08	150	70	50		60.0	30.0	2	0.60	5.2	0.4	2.06E+11	1.52E+09	8.88E+10	1.25E+09
13.95%	9.0	7.93	0.24	1.4	0.06	180	60	50		55.0	27.5	2	0.58	13.6	0.7	2.70E+11	1.98E+09	3.93E+11	4.21E+09
26.72%	4.3	3.40	0.17	0.5	0.05	200	60	50		55.0	27.5	2	0.59	5.8	0.3	3.01E+11	2.21E+09	1.45E+11	1.86E+09

Garfagnoli, F., Menna, F., Pandeli, E., Principi, G., 2005. The Porto Azzurro Unit (Mt. Calamita promontory, south-eastern Elba Island, Tuscany): stratigraphic, tectonic and metamorphic evolution. Boll. Soc. Geol. Ital. 3, 119–138.

Gibbs, A.D., 1990. Linked fault families in basin formation. J. Struct. Geol. 12, 795–803.

Gonzáles Guillot, M., Ghiglione, M., Escayola, M., Martins Pimentel, M., Mortensen, J., Acevedo, R., 2018. Ushuaia pluton: magma diversification, emplacement and relation with regional tectonics in the southernmost Andes. J. S. Am. Earth Sci. 88, 497–519.

Handy, M.R., Schmid, S.M., Bousquet, R., Kissling, E., Bernoulli, D., 2010. Reconciling plate-tectonic reconstructions of Alpine Tethys with the geological-geophysical record of spreading and subduction in the Alps. Earth Sci. Rev. 102 (3–4), 121–158.

Harrison, T.M., Duncan, I., McDougall, I., 1985. Diffusion of ^{40}Ar in biotite: temperature, pressure and compositional effects. Geochem. Cosmochim. Acta 49, 2461–2468.

Hiess, J., Condon, D.J., McLean, N., Noble, S.R., 2012. ^{238}U/^{235}U systematics in terrestrial uranium-bearing minerals. Science 335 (6076), 1610–1614.

Horstwood, M.S., Foster, G.L., Parrish, R.R., Noble, S.R., Nowell, G.M., 2003. Common-Pb corrected in situ U–Pb accessory mineral geochronology by LA-MC-ICP-MS. J. Anal. Atomic Spectrom. 18, 837–846. https://doi.org/10.1039/B304365G.

Ishii, K., Kanagawa, K., Shigematsu, N., Okudaira, T., 2007. High ductility of K-feldspar and development of granitic banded ultramylonite in the Ryoke metamorphic belt, SW Japan. J. Struct. Geol. 29, 1083–1098. https://doi.org/10.1016/j.jsg.2007.02.008.

Jackson, S.E., Pearson, N.J., Griffin, W.L., Belousova, E.A., 2004. The application of laser ablation-inductively coupled plasma-mass spectrometry to in situ U-Pb zircon geochronology. Chem. Geol. 211 (1–2), 47–69. https://doi.org/10.1016/j.chemgeo.2004.06.017.

Keller, J.V.A., Pialli, G., 1990. Tectonics of the Island of Elba: a reappraisal. Boll. Soc. Geol. Ital. 109, 413–425.

Kruhl, J.H., 1998. Reply. Prism- and basal-plane parallel subgrain boundaries in quartz: a microstructural geothermobarometer. J. Metamorph. Geol. 16, 141–146.

Le Breton, E., Handy, M.R., Molli, G., Ustaszewski, K., 2017. Post-20 Ma motion of the Adriatic plate: new constraints from surrounding orogens and implications for crust-mantle decoupling. Tectonics 36 (12), 3135–3154.

Liotta, D., Brogi, A., 2020. Pliocene-Quaternary fault kinematics in the Larderello geothermal area (Italy): insights for the interpretation of the present stress field. Geothermics 83, 101714. https://doi.org/10.1016/j.geothermics.2019.101714.

Liotta, D., Brogi, A., Meccheri, M., Dini, A., Bianco, C., Ruggieri, G., 2015. Coexistence of low-angle normal and high-angle strike- to oblique-slip faults during Late Miocene mineralization in eastern Elba Island (Italy). Tectonophysics 660, 17–34.

Liotta, D., Ruggieri, G., Brogi, A., Fulignati, P., Dini, A., Nardini, I., 2010. Migration of geothermal fluids in extensional terrains: the ore deposits of the Boccheggiano-Montieri area (southern Tuscany, Italy). Int. J. Earth Sci. 99, 623–644.

Lister, G.S., 1981. The effect of basal-prism mechanism switch on fabric development during plastic deformation of quartzite. J. Struct. Geol. 3, 67–75.

Lister, G.S., Davis, G.A., 1989. The origin of metamorphic core complexes and detachment faults formed during Tertiary continental extension in the northern Colorado River region. U.S.A. Journal of Structural Geology 11, 65–94.

Liu, H., Chen, Y., Wang, B., Faure, M., Erdmann, S., Martelet, G., Scaillet, B., Huang, F., 2020. Role of inherited structure on granite emplacement: an example from the Late Jurassic Shibei pluton in the Wuyishan area (South China) and its tectonic implications. Tectonophysics 779, 228394. https://doi.org/10.1016/j.tecto.2020.228394.

Locardi, E., Nicolich, R., 1992. Geodinamica del Tirreno e dell'Appennino centro-meridionale: la nuova carta della Moho. Mem. Soc. Geol. It. 41, 121–140.

Ludwig, K.R., 2003. User's Manual for Isoplot 3.00: A Geochronological Toolkit for Microsoft Excel. Kenneth R. Ludwig, Berkeley Geochronology Center, vol. 4. Spec. Publ., p. 74

Maineri, C., Benvenuti, M., Costagliola, P., Dini, A., Lattanzi, P., Ruggieri, G., Villa, I., 2003. Sericitic alteration at the La Crocetta deposit (Elba Island, Italy): interplay between magmatism, tectonics and hydrothermal activity. Miner. Deposita 38, 67–86.

Mainprice, D., Bouchez, J.-L., Blumenfeld, Ph, Tubià, J.M., 1986. Dominant *c* slip in naturally deformed quartz: implications for dramatic plastic softening at high temperatures. Geology 14, 819–822.

Marinelli, G., 1959. Le intrusioni terziare dell'isola d'Elba. Atti Soc. Toscana Sci. Nat. Pisa, Mem, Ser A LXVI (I), 50–253.

Martini, I.P., Sagri, M., 1993. Tectono-sedimentary characteristics of late miocene-quaternary extensional basins of the northern Apennines, Italy. Earth Sci. Rev. 34, 197–233.

Meesters, A.G.C.A., Dunai, T.J., 2002. Solving the production-diffusion equation for finite diffusion domains of various shapes: Part I. Implications for low-temperature (U-Th)/He thermochronology. Chem. Geol. 186 (3–4), 333–344.

Milano, M., Pierri, I., Florio, G., Cella, F., Fedi, M., 2019. Bouguer gravity field of the Tuscan archipelago (central Italy). J. Maps 15 (2), 751–758. https://doi.org/10.1080/17445647.2019.1669499.

Molli, G., 2008. Northern Apennine-Corsica orogenic system: an updated overview. Geological Society, London, Special Publications 298, 413–442.

Moyen, J.-F., Martin, H., Jayananda, M., Auvray, B., 2003. Late Archaean granites: a typology based on the dharwar Craton (India). Precambrian Res. 127, 103–123.

Musumeci, G., Mazzarini, F., Tiepolo, M., Di Vincenzo, G., 2011. U–Pb and ^{40}Ar–^{39}Ar geochronology of Palaeozoic units in the Northern Apennines: determining protolith age and alpine evolution using the Calamita Schist and Ortano Porphyroids. Geol. J. 46, 288–310.

Okudaira, T., Takeshita, T., Toriumi, M., 1998. Prism- and basal-plane parallel subgrain boundaries in quartz: a microstructural geothermobarometer. Discussion. J. Metamorph. Geol. 16, 141–146.

Pandeli, E., Giusti, R., Elter, F.M., Orlando, A., Orti, L., 2018. Structural setting and metamorphic evolution of a contact aureole: the example of the Mt. Capanne pluton (Elba Island, Tuscany, Italy). Ofiliti 43, 41–73.

Papeschi, S., Musumeci, G., Mazzarini, F., 2017. Heterogeneous brittle-ductile deformation at shallow crustal levels under high thermal conditions: the case of a syn-kinematic contact aureole in the inner northern Apennines, southeastern Elba Island. Italy. Tectonophysics 717, 547–564.

Pascucci, V., Martini, I.P., Sagri, M., Sandrelli, F., 2007. Effects of transverse structural lineaments on the Neogene-Quaternary basins of Tuscany (inner Northern Apennines, Italy). In: Nichols, G., Williams, E., Paola, C. (Eds.), Sedimentary Processes, Environments and Basins: a Tribute to Peter Friend. Intern. Ass. Sediment., vol. 38. Spec. Publ., pp. 155–182

Passchier, C.W., Trouw, R.A.J., 2005. Microtectonics, 2nd Revised and Enlarged Edition. Springer Verlag, p. 366.

Paterson, J.W., Newton, R.C., 1989. Reversed experiments on Biotite-Quartz-Feldspar melting in the system Kmash: implication for crustal anatexis. J. Geol. 97 (4), 465–485.

Peccerillo, A., 2003. Plio-quaternary magmatism in Italy. Episodes 26, 222–226.

Pertusati, P.C., Raggi, G., Ricci, C.A., Duranti, S., Palmeri, R., 1993. Evoluzione post-collisionale dell'Elba centro-orientale. Mem. Soc. Geol. Ital. 49, 297–312.

Prol-Ledesma, R.M., Morán-Zenteno, D.J., 2019. Heat flow and geothermal provinces in Mexico. Geothermics 78, 183–200. https://doi.org/10.1016/j.geothermics.2018.12.009.

Pryer, L.L., 1993. Microstructures in feldspars from a major crustal thrust zone: the Grenville Front, Ontario, Canada. J. Struct. Geol. 15 (1), 21–36.

Ranalli, G., 1995. Rheology of the Earth, second ed. Chapman and Hall, p. 413.

Rey, P.F., Teyssier, C., Whitney, D.L., 2009. Extension rates, crustal melting, and core complex dynamics. Geological Society of America 37 (5), 391–394.

Rossetti, F., Glodny, J., Theye, T., Maggi, M., 2015. Pressure-temperature-deformation-time of the ductile Alpine shearing in Corsica: from orogenic construction to collapse. Lithos 218–219, 99–116.

Rossetti, F., Tecce, F., Billi, A., Brilli, M., 2007. Patterns of fluid flow in the contact aureole of the late Miocene Monte Capanne pluton (Elba Island, Italy). The role of structures and rheology: Contrib. Mineral. Petrol. 153, 743–760.

Rowland, J.V., Sibson, R.H., 2004. Structural controls on hydrothermal flow in a segmented rift system Taupo Volcanic Zone, New Zealand. Geofluids 4, 259–283.

Scandale, E., Gandais, M., Willaime, C., 1983. Transmission electron microscopy study of experimentally deformed K-feldspar single crystals. The (010)[001], (001)1/2 [-112] and (1-11)1/2 [110] slip systems. Phys. Chem. Miner. 9, 182–187.

Schmid, S.M., Casey, M., 1986. Complete fabric analysis of some commonly observed *c*-axis patterns. Mineral and Rock Deformation: laboratory Studies - the Paterson Volume. Geophysical Monograph 36, 263–286.

Serri, G., Innocenti, F., Manetti, P., 1993. Geochemical and petrological evidence of the subduction of delaminated Adriatic continental lithosphere in the genesis of the Neogene-Quaternary magmatism of central Italy. Tectonophysics 223, 117–214.

Sibson, R.H., 1974. Frictional constraints on thrust, wrench and normal faults. Nature 249, 542–544.

Sibson, R.H., 2000. Fluid involvement in normal faulting. J. Geodyn. 29, 469–499.

Skipton, D.R., Warren, C.J., Hanke, F., 2018. Numerical modeling of P-T, time and grain-size controls on Ar diffusion in biotite: an aide to interpreting ^{40}Ar/^{39}Ar ages. Chem. Geol. 496, 14–24.

Smith, S.A.F., Holdsworth, R.E., Collettini, R.E., 2011. Interactions between plutonism and low-angle normal faults in the upper crust: insights from the Island of Elba. Italy. Geol. Soc. Am. Bull. 123, 329–346.

Spina, A., Capezzuoli, E., Brogi, A., Cirilli, S., Liotta, D., 2019. Mid- to late Permian microfloristic evidence in the metamorphic successions of Northern Apennines: insights for age-constraining and palaeogeographical correlations. J. Geol. Soc. 176 (6), 1262–1272. https://doi.org/10.1144/jgs2018-202.

Thomson, S.N., Brandon, M.T., Reiners, P.W., Zattin, M., Isaacson, P.J., Balestrieri, M.L., 2010. Thermochronologic evidence for orogen-parallel variability in wedge kinematics during extending convergent orogenesis of the northern Apennines, Italy. GSA Bullettin 122, 1160–1179.

Tullis, J., Christie, J.M., Griggs, D.T., 1973. Microstructures and preferred orientations of experimentally deformed quartzites. Geol. Soc. Am. Bull. 84, 297–314.

Van Achterbergh, E., Ryan, C.G., Jackson, S.E., Griffin, W.L., 2001. Data reduction software for LA-ICP-MS. Laser-Ablation-ICPMS in the earth sciences-Principles and applications. Miner. Assoc. Can. 29, 239–243.

Vermeesch, P., 2018. IsoplotR: a free and open toolbox for geochronology. Geoscience Frontiers 9, 1479–1493. https://doi.org/10.1016/j.gsf.2018.04.001.

Viti, C., Brogi, A., Liotta, D., Mugnaioli, E., Spiess, R., Dini, A., Zucchi, M., Vannuccini, G., 2016. Seismic slip recorded in tourmaline fault mirrors from Elba Island (Italy). J. Struct. Geol. 86, 1–12.

Wang, X., Griffin, W.L., Chen, J., Huang, P., Li, X., 2011. U and Th contents and Th/U ratios of zircon in felsic and mafic magmatic rocks: improved zircon-melt distribution coefficients. Acta Geol. Sin. 85, 164–174. https://doi.org/10.1111/j.1755-6724.2011.00387.x.

Westerman, D.S., Dini, A., Innocenti, F., Rocchi, S., 2004. Rise and fall of a nested Christmas-tree laccolith complex, Elba Island, Italy. In: Breitkreuz, C., Petford, N. (Eds.), Physical Geology of High-Level Magmatic Systems, Geol. Soc., vol. 234. Spec. Publ., London, pp. 195–213.

Widenbeck, M., Alle, P., Corfu, F., Griffin, W.L., Meier, M., Ober, F., Von Quant, A., Roddick, J.C., Spiegel, J., 1995. Three natural zircon standards for U-Th-Pb, Lu-Hf, trace element and REE analysis. Geostand. Newsl. 19, 1–23.

Willaime, Ch, Christie, J.M., Kovacs, M.-P., 1979. Experimental deformation of K-feldspar single crystals. Bull. Mineral. 102, 168–177.

Wu, L.-Y., Stuart, F.M., Di Nicola, L., Heizler, M., Benvenuti, M., Hu, R.-Z., 2019. Multi-aliquot method for determining (U+Th)/He ages of hydrothermal hematite: returning to Elba. Chem. Geol. 504, 151–157, 2019.

Zucchi, M., Brogi, A., Liotta, D., Rimondi, V., Ruggieri, G., Montegrossi, G., Caggianelli, A., Dini, A., 2017. Permeability and hydraulic conductivity of faulted micaschist in the eastern Elba Island exhumed geothermal system (Tyrrhenian sea, Italy): insights from Cala Stagnone. Geothermics 70, 125–145.